The Influence of Deep Cumulus Convection on Sea Breeze Dynamics Over South Florida
Part I: Model Development

by
J.L. Song and R.A. Pielke

Department of Atmospheric Science
Colorado State University
Fort Collins, Colorado

Colorado State University

Department of
Atmospheric Science

The Influence of Deep Cumulus Convection on Sea Breeze Dynamics Over South Florida
Part I: Model Development

by

J.L. Song and R.A. Pielke
Department of Atmospheric Science
Colorado State University
Fort Collins, Colorado 80523

May 16, 1988

Table of Contents

List of Figures

i

List of Tables

Abstract

Mesoscale - Convective interactions in Florida's sea breeze environment are investigated using a numerical approach with supportive observations. A hydrostatic primitive-equation model, originally developed by Pielke (1974), is coupled with a newly derived cumulus parameterization. The parameterization is designed to be as interactive as possible between the resolvable and the parameterized fields, while retaining the validity of a steady-state assumption over two distinct periods during the convective lifetime. During the first period, convective downdrafts are assumed to have not yet reached the subcloud layer, while during the second period the convective downdrafts produce both enhanced subsequent convection as well as surface stabilization. Convective lifetime is defined as one or more combinations of the two periods until the grid element is sufficiently stabilized. At the end of each period, the resolvable-scale dynamic and thermodynamic fields are updated in response to the convective feedback effects, therefore convection in the second period is associated with the updated resolvable-scale forcing. Height of maximum updraft mass flux is assumed to be a function of the degree of convective stabilization over the grid volume on the resolvable-scale previously determined. Downdrafts are assumed to initiate around the minimum-θ^e level, with mass fluxes increase at the same rate as updrafts. The water budget of the parameterization basically resembles that of Fritsch and Chappell (1980). Selected one-dimensional sensitivity tests of the parameterization are included in this study. In the accompanying paper (Song and Pielke, 1987), the parameterization is tested and discussed regarding its performance in simulating Florida's summertime sea breeze-convective interactions.

1 Introduction

The complicated interrelationship between deep cumulus convection and the associated at-mospheric regional/mesoscale circulations has been studied rather extensively during the last decade. Yet, due to limited physical understanding and computational resources, knowledge regarding the interrelationship is incomplete.

The difficulty in numerically simulating mesoscale-convective systems arises when observations suggest that mesoscale circulations (in particular, the divergent wind field) responds to convective heating rapidly and significantly (Frank, 1983). Thus, there is no clear scale-separation between deep cumulus convection and its mesoscale environment in terms of both space and time scales.

Practically, there are currently two types of numerical approaches for the purpose of simulating meso-β scale convective systems (i.e., domain sizes of about 200 km $\times$ 200 km):

(a) parameterizing deep convective effects in a hydrostatic mesoscale model and directly resolving the mesoscale system using a grid spacing of about 20 km;

(b) explicitly resolving both deep convection and the mesoscale system in a non-hydrostatic model with a grid spacing of about 1 - 2 km.

The advantage of the former is that it is currently available (Fritsch and Chappell, 1980; Zhang, 1985, Frank and Cohen, 1985), while its disadvantage is that the numerical technique is dependent upon a set of assumptions used in designing the parameterization. The advantage of the latter is that it directly resolves the desired four-dimensional mesoscale convective interactions. The disadvantage of approach (b) concerns the lack of observational data consistent with the 1 - 2 km model resolution, as well as the large computer resource requirements. Theoretically, a high-resolution simulation which directly resolves cumulus convection provides an extra advantage in that it offers a method to evaluate a cumulus parameterization scheme. However, the evaluation becomes unaffordable when, in addition

1

to the initialization and the verification problem, a domain of order 1000 km × 1000 km is required to represent the mesoscale system.

This study applies approach (a) to investigate the deep cumulus/mesoscale interactions in the summertime Florida environment, using the hydrostatic mesoscale primitive-equation model originally developed by Pielke (1974), together with a newly derived cumulus parameterization. Approach (b) is being used by the authors to improve on and to justify the cumulus parameterization approach and that result will be reported in a paper to be submitted.

The mesoscale environment of summertime Florida (in which the large-scale forcing is typically weak) is chosen for the study. The interactions between Florida's coastal deep convection and the mesoscale sea-breeze circulation over the peninsular-scale space domain and over the diurnal time period are simulated and discussed using the parameterization approach. The Florida peninsula-scale relationship between the early morning large-scale kinematic and thermodynamic properties and the afternoon surface rainfall was discussed recently by Burpee and Lahiff (1984). In particular, the early morning mid-tropospheric (700 - 500 mb) relative humidity is related to the timing of the afternoon peak rainfall as well as the vertical profile of the horizontal-averaged divergence. It was qualitatively stated that the reduction of the peninsula-scale surface convergence during late afternoon with a morning cooler and moister mid-troposphere is due to the combination of (1) downdraft cooling at the surface; (2) cirrus cover which reduces solar radiation; and (3) the stabilization produced by the mid/low tropospheric descent.

This atmospheric characteristic is generally consistent for a synoptically undisturbed day with the Florida convective characteristics documented in Byers and Braham (1949), Frank *et al.* (1967), Pielke (1974), Ulanski and Garstang (1978), Simpson *et al.* (1980), Cunning *et al.* (1982), Cooper *et al.* (1982), Watson and Blanchard (1984) as well as with the tropical convective studies of Gamache and Houze (1982) and Johnson and Kriete

(1982). However, a quantitative illustration of the intermediate processes which produce the afternoon atmospheric response has not been documented thus far in the literature. In fact, Burpee and Lahiff (1984) concluded their study by pointing out that "many of the important physical processes linking the different scales are still not well understood".

Various recent investigations have shown that there is generally not a clear-cut scale-separation between deep convection and its larger scale environment; rather, there are mesoscale moist and dry circulations accompanying the convection which link the mesoscale and deep cumulonimbus scale systems (Zipser, 1977; Ogura and Liou, 1980; Houze and Betts, 1982; Leary and Rappaport, 1987; among others). Johnson (1985) discussed the important implication of such a finding upon the cumulus parameterization problem. Frank and Cohen (1985) recognized that for simulating mesoscale convective systems, the mesoscale model resolution must be refined enough to resolve the accompanying deep cumulus induced mesoscale circulation, meanwhile the cumulus parameterization provides the feedback effects from the convective updrafts and downdrafts. Therefore, since we can not yet afford resolving mesoscale-convective systems over the Florida peninsula using a 1 km grid, the mesoscale grid-resolution used in Fritsch and Chappell (1980) and Frank and Cohen (1985) (i.e., a grid spacing of about 20 km) is applied in this study.

It is the major purpose of the current study (presented in this paper and in Song and Pielke, 1987, hereafter referred to as Part II) to quantitatively document the mesoscale-convective interactions in peninsular Florida which plays the essential role in converting the sea breeze forcing into convective rainfall. Along with this goal, we also investigate the feasibility and the overall acceptability of using a newly derived cumulus parameterization which is designed to be as interactive as possible with the mesoscale prognostic model.

Section 2 describes in detail the convective parameterization technique together with a listing of equations in the mesoscale prognostic model. The intercommunication between the parameterized convective heating and the resolvable-scale vertical motion is included at

the end of the section, showing how the deep convective feedback effects are incorporated into the mesoscale model during its execution. In Section 3, the cumulus parameterization used in the present study is examined in terms of its conservation of moist static energy and total water substance. In addition, one-dimensional sensitivity tests are performed which provide diagnostic knowledge regarding the performance of the current parameterization. Sensitivities due to the specified entrainment rate, precipitation efficiency, etc., are discussed. Finally, Section 4 summarizes the main assumptions used in designing the cumulus parameterization and the background knowledge as to why the assumptions are made. In the accompanying paper (Part II), the model is fully tested and discussed regarding its ability and shortcomings of simulating Florida's sea breeze-induced deep convective activities.

2   Numerical Technique

2.1   Mesoscale Model

The structure and numerical aspects of the mesoscale prognostic model, with the exception of the cumulus parameterization, has been described in detail in Pielke (1974), Mahrer and Pielke (1976, 1977, 1978), Pielke and Mahrer (1975, 1978), McNider and Pielke (1981), Pielke (1984) and Song *et al.* (1985). Since there is practically no change (except that the vertical domain was raised from 5 km to 20 km, and the incompressible assumption of representing the conservation of mass was replaced with an anelastic form), the governing equations are listed in Appendix A.

2.2   Convective Parameterization Technique

In the mesoscale prognostic model (in which cumulus feedback effects are incorporated), the Eulerian changes of potential temperature and specific humidity are given as (symbols used in the prognostic model equations are explained in Appendix A, while those used in the parameterization are explained in the text of this section):

4

$$\frac{\partial \bar{\theta}}{\partial t} = -\bar{v}_2 \cdot \nabla \bar{\theta} - \bar{w}\frac{\partial \bar{\theta}}{\partial z} + \frac{\partial}{\partial z}\left(K_z^\theta \frac{\partial \bar{\theta}}{\partial z}\right) + H_\theta + \left.\frac{\delta \bar{\theta}}{\partial t}\right|_R + \left.\frac{\delta \bar{\theta}}{\partial t}\right|_C \qquad (1)$$

and

$$\frac{\partial \bar{q}}{\partial t} = -\bar{v}_2 \cdot \nabla \bar{q} - \bar{w}\frac{\partial \bar{q}}{\partial z} + \frac{\partial}{\partial z}\left(K_z^q \frac{\partial \bar{q}}{\partial z}\right) + H_q + \left.\frac{\delta \bar{q}}{\partial t}\right|_C \qquad (2)$$

The deep cumulus convective feedback effects are included in the last term of each equation. Using the convective parameterization, these two terms are evaluated by

$$\left.\frac{\delta \bar{\theta}}{\delta t}\right|_C (Z) = \frac{\hat{\theta}(Z) - \theta_o(Z)}{\tau_c} \quad ; \quad \left.\frac{\delta \bar{q}}{\delta t}\right|_C (Z) = \frac{\hat{q}(Z) - q_o(Z)}{\tau_c} \qquad (3)$$

where θ_o, q_o = input from the grid scale field,

$\hat{\theta}, \hat{q}$ = output from the parameterization, and

τ_c = convective time period over which the feedback effects are incorporated (to be defined later in this section).

As in Fritsch and Chappell (1980), the grid-element adjustments due to convective effects are the weighted averaged defined below:

$$\hat{\theta}(z) = A^{-1}\left[\theta_E(z)A_E(z) + \theta_U(z)A_U(z) + \theta_D(z)A_D(z)\right] \qquad (4)$$

$$\hat{q}(z) = A^{-1}\left[q_E(z)A_E(z) + q_U(z)A_U(z) + q_D(z)A_D(z)\right] \qquad (5)$$

where the grid area $A = A_E + A_U + A_D$, and the subscripts $E, U,$ and D identify, respectively, grid-environment, updraft, and downdraft. The "grid-environment" is defined to be the three-dimensional space within a grid volume excluding the updraft and downdraft.

5

Therefore, the purpose of the parameterization is to evaluate $\theta_U(z)$, $q_U(z)$, $A_U(z)$, $\theta_D(z)$, $q_D(z)$, $A_D(z)$, $\theta_E(z)$ and $q_E(z)$, after every amount of time, τ_c, during the execution of the mesoscale prognostic model. The computational logic incorporated in the current parameterization follows the general approach applied in currently available cumulus parameterizations (as summarized in Frank, 1983). In particular, Fritsch and Chappell (1980) and Frank and Cohen (1985) provided the basis of deriving the current parameterization used in this study.

2.2.1 Convective Updraft

At a grid point, potential buoyant energy is first checked to see if its net value is positive. The source air of convective updrafts is defined as the mixture of the most unstable layer (500 m - 1000 m thick) within the lowest 2 km. Using the formulation of Bolton (1980), cloud base is defined as the lifting condensation level (LCL). Grid-scale mass flux at the cloud base must be positive in order to generate any convection. During the mature stage, convective downdraft mass flux contribute to the triggering of new convection such that its mass flux is added to the grid-scale mass flux (shown below).

Convective mass flux at cloud base is defined in such a way as to incorporate the quasi-time-dependent convective feedback effects. Following the formulations of Brown (1979) and Frank and Cohen (1985), updraft mass flux (M_U) at cloud base is defined as:

$$M_U(LCL) = \bar{M}(LCL) + \beta \cdot |M_D(LCL)|, \tag{6}$$

where $\bar{M} = $ resolvable-scale mass flux (must be positive to develop deep clouds),

$M_D = $ convective downdraft mass flux

$$\beta = \begin{cases} 0 \text{ for a "developing stage" (to be defined in this section)} \\ 1 \text{ for a "mature stage" (to be defined in this section).} \end{cases} \tag{7}$$

In the parameterization calculations, the "developing stage" refers to the earlier portion of deep convection where convective downdrafts have not yet reached the subcloud layer (the length of this stage is τ_c), while the "mature stage" is the period of time with the same length (τ_c) following the developing stage. The total lifetime of deep convection is the combination of one or more pair of developing and mature stages. The magnitude of τ_c is assumed to be the typical amount of time required for the mid-tropospheric initiated downdrafts to reach the surface. It is assumed that τ_c is long enough to include several downdraft effects (outflow, surface stabilization, etc.) and yet short enough that within it the steady state assumption is valid. Thus, τ_c = 20 minutes is used.

For the developing stage of deep convection, the updraft mass flux at cloud base is determined uniquely by the instantaneous grid-scale horizontal mass convergence within the subcloud layer. The convective downdraft outflow effects (Fritsch and Chappell, 1980) are not included during this stage.

After this developing stage, convective downdraft mass fluxes enter into the subcloud layer, such that the subsequent updraft mass flux is enhanced due to the three-dimensional mass convergence in the subcloud layer. Such a convective enhancement is similar to the well-known storm outflow effect, or gust-front convergence (Byers and Braham, 1949; Fujita, 1959; Charba and Sasaki, 1971; Ulanski and Garstang, 1978; Purdom, 1976; Simpson et al., 1980; Klemp et al., 1981; and Cooper et al., 1982). In the current parameterization scheme, this convective enhancement is explicitly incorporated in the calculation of convective feedback effects. Fig. 1 shows the flow-chart of the current parameterization. For example, the "RATIO" term (step-9 in Fig. 1) is defined as dividing the "updated" updraft mass flux at the cloud base (i.e., the sum of mature-stage downdraft mass flux and the grid-scale mass flux at the cloud base) by the grid-scale mass flux at the cloud base (a similar definition can be found in Gamache and Houze, 1982).

7

Observationally, such a quasi-time-dependent characteristic of the convective downdraft effect, and the characteristic that convective downdrafts lag in time from the updrafts, is often found in Florida. A sinusoidal curve regarding convective updraft and downdraft mass fluxes (i.e., a surface divergence regime produced due to downdrafts follows a surface convergence regime which generates updrafts) can be consistently found in the Florida observations (Cunning et al., 1982; Cooper et al., 1982; Watson and Blanchard, 1984; among others). Quantitatively, Cunning and DeMaria (1986) and Cunning et al. (1986) provided evidence that the subsequent convective transport following the formation of a surface mesohigh (which was produced by downdrafts) is about doubled as compared with the convective transport before the downdrafts. The ratio of this enhancement, as shown in their analysis, is proportional to the ratio between the initial mesoscale mass transport and the combined mass transport of mesoscale and convective processes.

Once the initial updraft mass flux at cloud base is "parameterized" using the grid-scale forcing, the next fundamental procedure of cumulus parameterization is to represent the vertical distribution of the convective feedback effects (Frank, 1983). However, the grid-scale field provides no information as to how the convective-scale heating/moistening should be distributed in the vertical. Therefore, another assumption is necessary.

Fritsch and Chappell (1980) assumed the updraft mass flux doubles at the cloud top from its magnitude at cloud base (that is, a constant entrainment rate is applied over the entire cloud depth). Frank and Cohen (1985) allowed the convective mass profile to vary according to both the mass entrainment and the mass detrainment (for both the updraft and the downdraft).

In the current parameterization, we modified the Fritsch-Chappell assumption concerning the updraft mass profile by stressing that the updraft mass is doubled up to (instead of always the cloud top height) a height around the mid/upper troposphere which is a function of the degree of convective stabilization on the resolvable-scale previously determined over

the grid volume. Song and Frank (1983), in analyzing data for all three phases of GATE, found that the time variability of the height of maximum convective heating correlates with that of the surface stabilization (determined primarily by the downdraft cooling effect). In the current parameterization, our assumption regarding the updraft mass profile results in a correlation similar to that documented in Song and Frank (1983). The computational procedure is illustrated below. Hereafter, we denote this height as the level of maximum updraft mass flux, or LMF. Below this height, the updraft entrains the environmental air at the specified rate. No detrainment is included in the mid/low-troposphere, since various observational and numerical studies (such as Klemp *et al.*, 1981) have indicated that deep convection is subject to profound lateral entrainment over the layer within about 3 - 5 km above the cloud base. Above the height of the LMF, the rising air mass decelerates and evolves into relatively significant horizontal displacement.

Since both the updraft and the downdraft are "one-dimensional" (i.e., only in the vertical) computationally, the horizontal mass divergence (i.e., detrainment) must necessarily reduce the updraft mass for the layer above the LMF in order to fulfill the level-by-level mass conservation. Therefore, conceptually there are two components in the mid/upper-troposphere over the grid volume: the convective updraft and the "anvil" cloud (i.e., the mass detrained from the updraft which occupies the grid-environment). The convective updraft maintains its coherent thermodynamic properties throughout its entire depth and occupies gradually smaller fractions of grid area as it approaches the cloud top. On the other hand, the anvil cloud has negligible vertical velocity over the layer between the cloud top and the LMF. The thermodynamic properties of the grid-environment in the layer are determined by the weighted mixture between the background mesoscale properties and those detrained from the updraft. In the current parameterization, since there is no grid-scale condensation (i.e., all moist processes are included in the cumulus parameterization),

the condensate in the anvil layer is required to evaporate/sublimate and saturate the grid-environment from the top level down.

Computationally, a two-step procedure is used to determine the updraft mass flux profile. When a deep convection is to be generated at a grid (i.e., there is upward mesoscale vertical velocity around the cloud base and a net potential buoyant energy), Bolton's (1980) formula (i.e., the simple Parcel method) is utilized to obtain the "positive area" on a SKEW-T diagram. The LMF is assigned the height of the maximum temperature excess on the "positive area". Once the LMF is assigned a value, the updraft mass profile can be determined according to the mass flux at the cloud base (Eq. 6) and the level-by-level calculations (shown below).

Following the notations used in Fritsch and Chappell (1980), the updraft mass flux profile is calculated by:

$$
\begin{aligned}
\Delta K_U(K) &= (Z(K+1) - Z(K))(Z_{LMF} - Z_{LCL})^{-1} \\
K_U(K) &= \sum_{q=LCL}^{q=K} \Delta K_U(q) \\
M_U(K) &= (1 + K_U(K)) M_U(LCL) \quad \text{for } LCL \leq K \leq LMF
\end{aligned}
\tag{8}
$$

$$
\begin{aligned}
\Delta K'_U(K) &= (Z(K+1) - Z(K))(Z_{KCT} - Z_{LMF})^{-1} \\
K'_U(K) &= \sum_{q=LMF}^{q=K} \Delta K'_U(q) \\
M_U(K) &= (1 - K'_U(K)) M_U(LMF) \quad \text{for } LMF < K \leq KCT,
\end{aligned}
\tag{9}
$$

where KCT and LMF denote the heights of cloud top and maximum updraft mass flux, respectively. Cloud top is defined as where updraft velocity vanishes. Therefore, as in Fritsch and Chappell (1980) and Zhang (1985), the updraft air above the temperature equilibrium level (if any) induces overshooting. In the current scheme, only clouds with depths greater than 3 km will be considered (STEP-3 of Fig. 1). Clouds with top heights lower than the middle troposphere are regarded as shallow cumulus clouds which are typically non-precipitating, and without significant downdrafts (Johnson, 1978).

The thermodynamic properties of the updraft are determined by considering isobaric mixing due to entrainment (note, entrainment is zero above the LMF), as given by:

$$\theta_U^e(K) = \left[\theta_U^e(K-1)M_U(K-1) + \Delta M_U(K-1)\tilde{\theta}_E^e(K-1)\right](M_U(K))^{-1}$$
$$q_U(K) = \left[q_U(K-1)M_U(K-1) + \Delta M_U(K-1)\tilde{q}_E(K-1)\right](M_U(K))^{-1} \quad (10)$$

where
$$\Delta M_U(K-1) = M_U(K) - M_U(K-1)$$
$$\tilde{\theta}_E^e(K-1) = 0.5 \star [\theta_E^e(K-1) + \theta_E^e(K)]$$
$$\theta^e = \text{equivalent potential temperature}$$
$$\tilde{q}_E(K-1) = 0.5 \star [q_E(K-1) + q_E(K)]$$

Once the buoyancy profile is determined, the updraft vertical velocities are calculated utilizing a simplified buoyancy equation (i.e., as in Fritsch and Chappell, 1980, the condensate loading effect is neglected):

$$W_U(K) = W_U(K-1) + \left[2 \star g \star \Delta Z(K) \star \frac{\tilde{\theta}_U^v(K) - \tilde{\theta}_E^v(K)}{\tilde{\theta}_E^v(K)}\right]^{1/2} \quad (11)$$

where
$$\Delta Z(K) = Z(K) - Z(K-1)$$
$$\theta_U^v, \theta_E^v = \text{virtual potential temperature of the updraft}$$
$$\text{and the grid environment, and}$$
$$\tilde{\theta}_U^v, \tilde{\theta}_E^v = \text{layer-averaged quantities as defined in Eq. 10.}$$

Assuming the pressure for each of the convective components (updraft or downdraft) is the same as that of the grid-element, the densities of the updraft and downdraft can be calculated. Thus, the vertical profile of updraft area is determined by:

$$A_U(K) = \frac{M_U(K)}{D_U(K) \cdot W_U(K)} \quad (12)$$

where D_U = updraft density.

The water budget of the current scheme is formulated following the method introduced in Fritsch and Chappell (1980). That is, microphysical processes are not considered. Instead, a precipitation efficiency function is used for the generation of rain. Using the formulation

11

in Fritsch and Chappell (1980) scheme, precipitation efficiency for the Florida (weakly-sheared) environment is found to be always about 90%, not changing with both time and horizontally. To simplify the computation, a constant value (about 70%) is used in the control run of the present study (discussed in Part II). Sensitivities of several parameterized convective effects due to the specified precipitation efficiencies are illustrated in Section 3. The computations of the level-by-level condensate production and consumption are exactly the same as in Fritsch and Chappell (1980) (see their Fig. 4 and Fig. 5). Minor changes are only made regarding the depths of the freezing and melting layers. That is, freezing is assumed to occur in a gradual manner over a layer between $T_U = -5°C$ and $T_U = -20°C$, while melting occurs within a 2 km-layer immediately beneath the $T_E = 0°C$ level.

2.2.2 Convective Downdraft

Various observational investigations (Zipser, 1977; Knupp, 1985) have indicated that convective downdrafts are closely related to mid-tropospheric low θ^e air. In the current scheme, a downdraft is assumed to initiate at the height where $\theta^e_E(K)$ is minimum.

The initial downdraft mass flux, following the formulation of Frank and Cohen (1985), is defined as

$$M_D(LDI) = \epsilon\, M_U(LCL) \tag{13}$$

where, $\epsilon = -0.5$ is used (discussed below), and
$LDI = $ level of downdraft initiation.

For the Florida area, Cooper et al. (1982) has suggested that near the surface the downdraft mass flux has a comparable (although somewhat smaller) magnitude as found for the updrafts (their Fig. 15). Therefore, assuming $\epsilon = -0.5$, together with the assumption that the downdraft mass flux doubles from LDI to the surface, provides a comparable (but somewhat smaller) downdraft mass flux (as compared with the updraft) at cloud base. It should be kept in mind that the convective feedback effects produced by the

12

downdrafts are determined by, in addition to the mass fluxes, also the thermodynamic properties of the downdraft and the updated grid-scale field (particularly during the mature stage). Consequently, downdraft mass fluxes are calculated by:

$$
\begin{aligned}
\Delta K_D(K) &= (Z(K) - Z(K-1))(Z(LDI) - Z(1))^{-1} \\
K_D(K) &= \sum_{q=LDI}^{q=K} \Delta K_D(q) \\
M_D(K) &= (1 + K_D(K))M_D(LDI)
\end{aligned}
\tag{14}
$$

The initial downdraft thermodynamic properties are determined by a mixture between updraft air and environmental air at the level of the LDI. The level-by-level isobaric mixing effects due to entrainment are calculated by

$$
\left.
\begin{aligned}
\theta_D^e(K) &= \left[\theta_D^e(K+1)M_D(K+1) + \Delta M_D(K) \star 0.5 \star \left(\tilde{\theta}_E^e(K) + \tilde{\theta}_U^e(K)\right)\right](M_D(K))^{-1} \\
q_D(K) &= \left[q_D(K+1)M_D(K+1) + \Delta M_D(K) \star 0.5 \star (\tilde{q}_E(K) + \tilde{q}_U(K))\right](M_D(K))^{-1}
\end{aligned}
\right\} \text{(LCL} \leq \text{K} \leq \text{LDI)}
\tag{15}
$$

$$
\left.
\begin{aligned}
\theta_D^e(K) &= \left[\theta_D^e(K+1)M_D(K+1) + \Delta M_D(K)\tilde{\theta}_E^e(K)\right](M_D(K))^{-1} \\
q_D(K) &= \left[q_D(K+1)M_D(K+1) + \Delta M_D(K)\tilde{q}_E(K)\right](M_D(K))^{-1}
\end{aligned}
\right\} \text{(1} \leq \text{K} \leq \text{LCL)}
\tag{16}
$$

It is seen that downdrafts entrain both updraft air and environmental air within the in-cloud layers (Eq. 15), but only the environmental air in the subcloud layer (Eq. 16).

Finally, downdraft velocities and areas are calculated by:

$$
W_D(K) = W_D(K+1) + \left[2 \star g \star \Delta Z(K) \star \frac{\tilde{\theta}_E^v(K) - \tilde{\theta}_D^v(K)}{\tilde{\theta}_E^v(K)}\right]^{1/2}
\tag{17}
$$

$$
A_D(K) = \frac{M_D(K)}{D_D(K)W_D(K)}
\tag{18}
$$

2.2.3 Grid-Environment

The downdraft outflow effect (i.e., the surface cooling due to the replacement of boundary layer unmodified air with the colder downdraft air) is considered only during the mature

state. In the mature state, the total downdraft mass entering the subcloud layer (m_{DB}) is defined by modifying the formulation of Fritsch and Chappell, (1980) to:

$$m_{DB} = -\beta \tau_c (D_D \quad \star \quad W_D \quad \star \quad A_D)_{LCL} \tag{19}$$

The mass needed to fill the layer K of a grid element (m_G) is

$$m_G(K) = \tilde{D}_D(K) \cdot \Delta Z(K) \cdot A \cdot \frac{(D_D W_D A_D)_{LCL}}{(D_D W_D A_D)_{LCL} + \left(\overline{DWA}\right)_{LCL}} \tag{20}$$

where β is defined in Eq. 7. The fraction of grid area and depth over which the downdraft replacement takes place is determined from m_{DB} and m_G.

Above the level of maximum updraft mass flux (LMF), detrained updraft air and water substance are horizontally mixed with the air in the grid environment. The detrained updraft mass occupies an area (A_{DET}) determined from the net mass convergence of updraft air above the LMF, i.e.,

$$A_{DET} = \tau_c \frac{M_U(K) - M_U(K+1)}{\tilde{D}_E(K) \cdot (Z(K+1) - Z(K))} \tag{21}$$

The modifications upon the grid-environment due to the detrainment are calculated by:

$$
\begin{aligned}
\theta_E^e(K) &= [\theta_E^e(K) \star (A_E(K) - A_{DET}) + \theta_U^e(K) \star A_{DET}] (A_E(K))^{-1} \\
q_E(K) &= [q_E(K) \star (A_E(K) - A_{DET}) + q_U(K) \star A_{DET}] (A_E(K))^{-1}
\end{aligned}
\tag{22}
$$

Evaporation or sublimation in the detrainment layer (i.e., the layer between LMF and cloud top) provides extra cooling and moistening in the upper troposphere.

Finally, the adiabatic warming associated with the compensating subsidence motion is calculated as follows:

14

$$W_E(K) = -[M_U(K) + M_D(K)] \ [D_E(K) \star A_E(K)]^{-1} \qquad (23)$$

$$\theta_E^e(K) = \theta_E^e(K) - \tau_c \star W_E(K) \star \frac{\theta_E^e(K+1) - \theta_E^e(K)}{Z(K+1) - Z(K)}$$

$$q_E(K) = q_E(K) - \tau_c \star W_E(K) \star \frac{q_E(K+1) - q_E(K)}{Z(K+1) - Z(K)} \qquad (24)$$

Note that an upstream differencing replaces the central differencing in the calculation of subsidence warming and drying (Eq. 24). Therefore, the recursive (and computationally expensive) procedure used in Fritsch and Chappell, (1980) is avoided; so is the computational instability associated with the central differencing.

In summary, the subgrid-scale convective feedback effects are calculated in the parameterization utilizing area-weighted averaging (Eqs. 4 and 5). For the developing stage, the required profiles are obtained from Eqs. 10, 12, 15 or 16, 18, 22 and 24. For the mature stage, the "RATIO" (Fig. 1) is calculated using the updated grid-scale mass flux at cloud base and the mature-stage downdraft mass flux at cloud base. The above profiles are then multiplied by the "RATIO" to determine the mature-stage convective feedback effects.

In order to illustrate the convective effect upon the resolvable-scale field, a grid point near the west coast at the latitude of Lake Okeechobee is chosen as an example. The mesoscale model input is illustrated in Fig. 2(a) and Fig. 2(b). During the time between 14:15 EST (19:15 GMT) and 16:02 EST there are five "clouds" simulated by the parameterization, separated by about 21 - 22 minutes. In the following Figs., the input grid-scale vertical velocity profile (Fig. 3a), the parameterized convective heating profile (Fig. 3b) and the convective moistening profile (Fig. 3c) are shown.

Before 14:15 EST, no cloud developed in this grid. Therefore, as seen in Fig. 3a, curve (1) indicates there is weak downward motion throughout the mid and upper troposphere (presumably due to compensating downward motion caused by neighboring convection) and weak upward motion in the lower troposphere due to sea breeze convergence. The first cloud

is initiated at 14:15 EST, which produces the convective heating profile shown as curve (1) in Fig. 3b. We see there is relatively weak heating (a peak value of $\sim$40°C/day) near 350 mb, and very weak cooling in the subcloud layer ($\sim$5°C/day). This cloud is in stage 1 as defined previously, therefore no downdraft cooling is incorporated.

The above heating is then incorporated into the mesoscale model for the following 20 minutes (equally divided into each time step). The resultant grid-scale vertical velocity after the 20 minutes is shown as curve (2) in Fig. 3a (at time 14:36 EST). It is seen that relatively very little change is made due to the weak heating. However, the next cloud, which represents the stage 2 convection, produces strong heating (a peak value of 113°C/day, near 325 mb) and strong cooling (−70°C/day in the subcloud layer and $\sim$−150°C/day at the surface as shown in the curve (2) of Fig. 3b; also a cooling of about −30°C/day around cloud top). The grid-scale response is shown as curve (3) in Fig. 3a. We see that significantly increased upward motion has become established on the resolvable-scale in the mid and upper troposphere (Fig. 3a).

The largest increase of the grid-scale vertical velocity is between 15:10 EST and 15:41 EST (i.e., from curve (4) to curve (5) in Fig. 3a). This is the result of the mature stage convective heating (as discussed in Houze, 1982; and Johnson and Kriete, 1982) shown as curve (4) in Fig. 3b. After this development, the grid element is stabilized (due to both the upper heating and the lower-level downdraft cooling). Therefore, curve (6) in Fig. 3a already indicates downward motion in the lower troposphere (i.e., the system is in a decaying stage). Accordingly, there is no new cloud initiated at this grid.

Fig. 3c shows that the deep convective effects provide important moistening over the layer between about 500 mb and 800 mb, and to a weaker degree around the tropopause (anvil evaporation and sublimation). The lower tropospheric convective moistening effect appears somewhat discontinuous which is due to the discontinuous computations of downdraft entrainment-mixing effects above and below the cloud base (Eqs. 15 and 16).

16

3 Parameterization Sensitivity Tests

Within a grid volume in which the cumulus parameterization is executed, the overall effect of cumulus convection is to redistribute sensible heat and water substance in the vertical, and to produce net condensation which generates rainfall. Because of this net condensation, there is net heating in the grid volume. Meanwhile, because the net condensation (i.e., rainfall) is assumed to exit the domain of the parameterization, there must be net drying in the domain. An exact correspondence among the three terms (net heating; surface rainfall; net drying) indicates conservation of both the moist static energy and water substance.

After the cumulus parameterization is performed in this study, an adjustment to assure the conservation is achieved by first requiring water substances to be balanced, and then requiring that the final net heating corresponds to the net condensation. An iterative procedure is used to reach the balance conditions. The condition for the convergences is such that the residuals are smaller than the involved quantities by at least two orders of magnitude.

An example of using an arbitrarily selected sounding is described in detail in Song (1986); only the results are shown here. In order to show the effect of requiring the conservation of both moist static energy and water substance in the parameterization, the heating/moistening are listed separately in Appendix B for the cases without (Appendix B-1) and with (Appendix B-2) the adjustment.

Comparing Appendix B-1 and Appendix B-2, we see that due to the iterations for requiring conservation, the maximum heating, for example, changes by only 0.3%. The maximum cooling at the surface changes by only a negligible amount (smaller than the second decimal point). Therefore, we see that the parameterized net heating is essentially conserved without the conservation readjustment.

Relatively larger effects appear only on the humidity quantities, but the absolute value of the residuals are still significantly smaller than the variation due to physical processes.

17

For example, both the mid-tropospheric moistening (at level 7) and surface drying are changed by only 0.6%. The only relatively large change is at cloud top (detrainment induced evaporational moistening), which changes by about 25%. Since moisture content is typically negligible at that height (14 km), the change is considered not important for the discussions of this study.

The sensitivities of the parameterization performance as a function of several of the assumptions used in the formulation of the scheme and different physical background are included in Song (1986), using both one-dimensional experiments and three-dimensional prognostic experiments. In the current study, the diagnosed sensitivities of the current parameterization to the entrainment rate; precipitation efficiency; downdraft initial temperature and humidity; downdraft initial mass flux; and downdraft relative humidity will be shown below. In each of the one-dimensional experiments, sensitivities are illustrated with respect to the convective heating and moistening and other relevant parameters over a 20-minute period (if not otherwise mentioned).

3.1 Sensitivity to Entrainment Rate

Entrainment rate is referred to as the rate of mass increase with height for the updraft (from the LCL to the LMF) or downdraft (from the LDI to the surface). In this subsection, three entrainment rates are considered for the sensitivity test: a zero-entrainment case (i.e., updraft mass and downdraft mass do not change with height) and two cases in which updraft and downdraft mass increase by 100% (i.e., doubling), and 300% (i.e., quadrupling). Fig. 4 shows the updraft mass flux profiles (calculated in Eqs. 8 and 9) for the zero-entrainment case (thin-solid line), the doubling case (thick-solid line) and the quadrupling case (dashed line). It is seen from Fig. 4 that the cloud tops for the former two cases reach about 15 km, while the cloud top for the quadrupling case is only around 10 - 11 km. Fig. 5 shows the vertical profiles obtained by subtracting the grid-environment potential temperature (Eqs. 22 and 24) from the updraft potential temperature (Eq. 10), for the same experiments as

in Fig. 4. We see from Fig. 5 that above the LMF (which is around 9 km), the updraft for the zero-entrainment case becomes significantly warmer than the grid-environment at the corresponding levels since no entrainment-induced dilution is incorporated for these levels. On the other hand, the quadrupling case shows too large a dilution for the updraft, resulting in a small buoyancy. It should be noted that the updrafts discussed here contain the freezing processes which the simple parcel method (used to locate the LMF) does not include.

The updraft velocities (calculated in Eq. 11) for the same cases are shown in Fig. 6. We see from Fig. 6 that except for the quadrupling case, in which the cloud depth is too small, the entrainment rate variability changes mainly the magnitude of the updraft velocity and less its vertical distribution. Similarly, the sensitivity of the downdraft velocities (Eq. 17) in the same cases is shown in Fig. 7. We see from Fig. 7 that the effect of changing the pre-specified entrainment rate is even smaller on the downdraft velocity than on the updraft velocity.

Fig. 8 shows the vertical velocities of the compensating motion in the grid-environment due to the convective mass fluxes (Eq. 23), for the three cases presented in Fig. 4. We see from Fig. 8 that the quadrupling case, although producing a shallower cloud due to large dilution, generates a strong updraft mass flux around the LMF (Fig. 4) and therefore strong subsidence velocity (Fig. 8). Such stronger subsiding motion produces larger adiabatic warming (Eq. 24) as compared with the less-entraining cases.

The final convective heating and moistening profiles (Eqs. 4 and 5) for the three cases are shown, respectively, in Figs. 9 and 10. We see from Fig. 9 that the different values of the pre-specified entrainment rate produces changes of the magnitude of the convective heating, especially around the maximum updraft mass flux level (near 9 km). Larger entrainment rates result in larger subsidence warming, due to larger updraft mass fluxes. However, large entrainment rates produce strong dilution, thereby reducing the updraft buoyancy

and, consequently, the cloud depth. Strong cooling due to updraft overshooting can be found around 11 km for the quadrupling case, and, to a lesser degree, around 15 - 16 km for the less-entrained cases. Fig. 10 shows that, as for the convective heating, the convective moistening vertical profile is not sensitive to the changes of the entrainment rate (except for the detrainment around cloud top). In summary, except for the possible overshooting-induced cooling and moistening near cloud top (which differ most significantly for the quadrupling case), the entrainment rate variability considered between the zero- and the doubling-assumption used in the sensitivity experiment does not change the main feature of the parameterized convective feedback effects.

3.2 Sensitivity to Precipitation Efficiency

In the current parameterization the pre-specified precipitation efficiency (PEF) affects the calculation of convective feedback effects through the melting and the anvil evaporation computations. Following Fritsch and Chappell (1980), the total precipitation of the convection is determined by multiplying the total moisture supply (i.e., total water flux averaged around the cloud base) by the PEF. A fraction of this total precipitation is ice (i.e., the condensate produced in the updraft above the $T_U = -20°C$ level, and in a gradual manner between the $T_U = -5°C$ and $T_U = -20°C$ levels, is ice), which is assumed to melt in the specified melting layer (a 2 km layer immediately below the $T_E = 0°C$ level). The amount of anvil evaporation is obtained by subtracting the downdraft evaporation from the total evaporation (the total evaporation is the residue of subtracting the total precipitation from the total condensate produced in the updraft). Also, as in Fritsch and Chappell (1980), the anvil evaporation or sublimation is assumed to saturate the grid-environment, starting from the top-most layer.

In the following sensitivity experiment (Table 3-1), precipitation efficiency (PEF) is varied using the values 10, 30, 50, 70 and 90%. It is seen from Table 3-1 that using a larger PEF results in a somewhat stronger downdraft (stronger cooling in the melting layer)

and somewhat weaker anvil evaporation (weaker cooling and moistening in the anvil layer) than using a smaller PEF. Ulanski and Garstang (1978) stated that for large storms in Florida the PEF may reach 72%, while for small storms the PEF may only be 37% (a statement which is further confirmed by Simpson et al., 1980, and Lopez et al., 1984, that the larger, or merged, systems are the more efficient rain producer). However, a proper functional relationship which relates the PEF with the mesoscale parameters (similar to that of Fritsch and Chappell, 1980) with respect to the Florida environment is not known. To determine the proper PEF, therefore, apparently requires the explicit cumulus field simulation approach together with consistent observations (as stated previously in this paper).

3.3 Sensitivity to Initial Downdraft Thermodynamic Property

At the downdraft initiation level, the initial downdraft temperature and humidity are assumed to be weighted averages between the updraft and the environment values. That is:

$$\begin{array}{c} Initial \\ downdraft \\ property \end{array} = \alpha \cdot \left(\begin{array}{c} environmental \\ property \end{array} \right) + (1 - \alpha) \cdot \left(\begin{array}{c} updraft \\ property \end{array} \right)$$

Table 3-2 shows the effects of changing the weighting factor α. Note the final surface cooling (column 3) is the weighted-average (calculated from Eq. 4) among the grid-element components including the downdraft contribution (column 2).

It is seen from Table 3-2 that between a "50-50 mixture" assumption (i.e., $\alpha = 50\%$) and the $\alpha = 90\%$ assumption, the final surface cooling differ by only about $0.5°C$. Therefore, the downdraft intensity is relatively insensitive to its initial thermodynamic property. Rather, as stated previously, the final downdraft effects depend on both the mass flux and the level-by-level entrainment-mixing effects.

3.4   Sensitivity to Initial Downdraft Mass Flux

To indicate how the downdraft effect depends on its initial mass flux (given the initial environmental thermodynamic profile indicated in Fig. 2b), the quantity ϵ in Eq. 13 was varied in steps of 20% between 10% and 90% in a set of sensitivity experiments. The influence of the different values of ϵ on the maximum parameterized cooling and drying are shown in Table 3-3.

It is seen from Table 3-3 that, with everything else in the parameterization the same, an initially stronger downdraft results in a stronger mass flux entering the subcloud layer (column 1); a larger area within the grid column (Eqs. 19 and 20) in which air is replaced by the downdraft air (column 2); and larger surface cooling (column 3) and drying (column 4) for the final convective feedback effects.

Knupp (1985) showed that for individual clouds the downdraft mass may increase to about 10 times from its magnitude at the initiation level (4 - 6 km above ground) to that near surface (0.5 - 0.8 km above ground) (see his Fig. 4.14); while for the storm-scale (30 km × 30 km) averaged-quantities, the downdraft mass fluxes at cloud base are comparable to, but somewhat smaller than, the updraft mass fluxes at cloud base (see his Fig. 4.7). For the latter case, it is shown that (for the 10 profiles he sampled) the updraft mass fluxes near 1 km are averaged to be about 1.5 times the averaged downdraft mass fluxes at the same height. Although Knupp's data is derived from a significantly different physical background (continental, cold-base convection), the above ratio (i.e., M_U/M_D at LCL) is not too different from that reported in Cooper *et al.* (1982) for the Florida convection (which showed that near the surface, M_U and M_D are comparable). Therefore, for the Florida simulations performed in this study, the downdraft mass flux is computed as in Eqs. 13 and 14.

3.5 Sensitivity to Downdraft Relative Humidity

In the current parameterization, a constant downdraft relative humidity (RHD) is assumed for both the cloud layer and the subcloud layer. In this sensitivity experiment, for a downdraft with $RHD \leq 50\%$, there is not enough cooling to sustain the downdraft to reach the subcloud layer. Therefore, only 70% and 90% are considered in the sensitivity test. Table 3-4 shows the effects of changing RHD.

It is seen that, for $RHD = 70\%$, there is relatively smaller cooling and larger drying in the surface layer; while for $RHD = 90\%$ there is larger cooling and smaller drying. The maximum difference is 1.4°C for cooling and 0.024 (g/kg) for drying. The basic convective feedback effects are not affected significantly as long as the convective downdrafts are "nearly-saturated" (Zipser, 1977). In the sea breeze simulations discussed in Part II, RHD = 80% is assumed.

4 Summary

Florida's summertime sea breeze-deep convective interactions are investigated using a numerical approach. A hydrostatic primitive-equation model, originally developed by Pielke (1974) and Pielke and Mahrer (1978), is coupled with a cumulus parameterization which is derived based on the discussions in Fritsch and Chappell (1980), Song and Frank (1983), and Frank and Cohen (1985). A detailed description of the model performance and discussion of results are included in an accompanying paper (Song and Pielke, 1987). In order to concisely distinguish the current cumulus parameterization from others, the main assumptions used in designing the parameterization and the background knowledge of why the assumptions are made are summarized below.

The first main assumption we made in the cumulus parameterization concerns the quasi-time-dependent formulation of the updraft mass flux at the cloud base. The meaning of this assumption is two-fold:

1. It avoids making the (another) assumption that the convective intensity is completely steady state over the whole period of the convective lifetime. The cited sinusoidal curve of surface convergence (which has been consistently documented in various Florida observational investigations, such as Cooper *et al.*, 1982) indicates that it is necessary to divide the convective lifetime into more than one distinct stage.

2. It stresses that the convectively self-generated downdraft massflux can provide a feedback effect such that subsequent convection is enhanced over what can initially be "predicted" using only the grid-scale information. The cited reference of Cunning and DeMaria (1986) discussed in detail the evidence which supports this assumption.

The second main assumption is the 20 min. used as the length for each of the stages. This length was determined by the consideration of:

1. The typical amount of time required for mid-tropospheric initiated downdrafts to reach the subcloud layer.

2. A time period long enough to include several downdraft effects (such as the outflow effect, surface stabilization effect) and yet short enough that within it the steady-state assumption is valid.

The third main assumption concerns the updraft mass flux profile (this largely determines the subsidence velocity profile). We made, first, the same assumption as in Fritsch and Chappell (1980) that the updraft mass doubles between cloud base and cloud top (which is shown to be a reasonable assumption according to our 1-D sensitivity test). However, we locate the maximum updraft massflux, instead of at the cloud top, at a height which is a function of the degree of convective stabilization on the grid-scale, previously determined over the grid volume. The meaning of this assumption is two-fold:

1. It inserts time-variability to the updraft mass profile, since the degree of convective stabilization varies with time;

2. (In association with the time-variability) it stresses the coexistence of the updraft and the "anvil" (or the detrainment cloud region). That is, the rising air mass expands horizontally as it approaches the cloud top. This "horizontal" portion of the rising air mass has negligible vertical motion and therefore can not be considered as "updraft". This means that the updraft mass decreases with height in this detrainment layer. Consequently, the compensating mass flux decreases in this layer (in order to fulfill the level-by-level mass conservation).

Finally, the fourth main assumption concerns the downdraft mass profile (which affects the lower tropospheric cooling intensity and its vertical variation). It must be realized that the convective downdraft is far less understood than the updraft. Fritsch and Chappell (1980) was the first modeling study which, in realizing the importance of the downdrafts, explicitly included downdraft effects into a cumulus parameterization used for mesoscale studies (that is, a weighted-average approach including updraft, downdraft and the grid-environment effects). Therefore, we followed them in several aspects in the downdraft calculation (such as the outflow effect). Our assumption of the downdraft mass profile was derived from two sources of experimental information:

1. Downdraft mass doubles between its source height and the surface when this "downdraft" is the sinking mass averaged over a storm-scale (30 km x 30 km) region. This information was obtained from Knupp (1985) where he analyzed data of continental cloud-base convection (CCOPE), and the downdrafts initiated primarily around the mid-troposphere (where θ^e is minimum).

2. (In association with the above assumption) we assumed the initial downdraft mass is 50% of the updraft mass at cloud base. Therefore, together with the doubling assumption, the downdraft mass is comparable to the updraft's near the surface (which is a reasonable assumption as shown by the Florida observational analysis of Cooper *et al.*, 1982).

25

6 References

Bolton, D., 1980: The computation of equivalent potential temperature. *Mon. Wea. Rev.*, **108**, 1046-1053.

Brown, J.M., 1979: Mesoscale unsaturated downdrafts driven by rainfall evaporation: A numerical study. *J. Atmos. Sci.*, **36**, 313-338.

Burpee, R.W. and L.N. Lahiff, 1984: Area averaged rainfall variations on sea-breeze days in south Florida. *Mon. Wea. Rev.*, **112**, 520-534.

Byers, H.R. and R.R. Braham, Jr., 1949: The Thunderstorm. U.S. Government Printing Office, Washington, D.C., 287 pp. [NTIS PB-234515].

Charba, J. and Y. Sasaki, 1971: Structure and movement of the severe thunderstorms of 3 April 1964 as revealed from radar and surface mesonetwork data analysis. *J. Meteor. Soc. Japan*, **49**, 191-213.

Cooper, H.J., M. Garstang and J. Simpson, 1982: The diurnal interaction between convection and peninsular-scale forcing over south Florida. *Mon. Wea. Rev.*, **110**, 486-503.

Cunning, J.B. and M. DeMaria, 1986: An investigation of the development of cumulonimbus systems over south Florida. Part I: Boundary layer interactions. *Mon. Wea. Rev.*, **114**, 5-24.

Cunning, J.B., R.L. Holle, P.T. Gannon and A.I. Watson, 1982: Convective evolution and merger in the FACE experimental area: Mesoscale convergence and boundary layer interaction. *J. Appl. Meteor.*, **21**, 953-977.

Cunning, J.B., W. Poor and M. DeMaria, 1986: An investigation of the development of cumulonimbus systems over south Florida. Part II: In-cloud structure. *Mon. Wea. Rev.*, **114**, 25-39.

Frank, N.L., P.L. Moore and G.E. Fisher, 1967: Summer shower distribution over the Florida peninsula as deduced from digitized radar data. *J. Appl. Meteor.*, **6**, 309-319.

Frank, W.M., 1983: The cumulus parameterization problem. *Mon. Wea. Rev.*, **111**, 1859-1871.

Frank, W.M. and C. Cohen, 1985: Properties of tropical cloud ensembles estimated using a cloud model and an observed updraft population. *J. Atmos. Sci.*, **42**, 1911-1928.

Fritsch, J.M. and C.F. Chappell, 1980: Numerical prediction of convectively driven mesoscale pressure systems. Part I: Convective parameterization. *J. Atmos. Sci.*, **37**, 1722-1733.

Fujita, T., 1959: Precipitation and cold air production in mesoscale thunderstorm systems. *J. Meteor.*, **16**, 454-466.

Gamache, J.F. and R.A. Houze, Jr., 1982: Mesoscale air motions associated with a tropical squall line. *Mon. Wea. Rev.*, **110**, 118-135.

Houze, R.A., Jr., 1982: Cloud clusters and large scale vertical motions in the tropics. *J. Meteor. Soc. Japan*, **60**, 396-409.

Houze, R.A. and A.K. Betts, 1981: Convection in GATE. *Rev. Geophys.*, **19**, 541-576.

Johnson, R.H., 1978: Characteristic structure and growth of the nonprecipitating cumulus layer over south Florida. *Mon. Wea. Rev.*, **106**, 1495-1504.

Johnson, R.H. and D.C. Kriete, 1982: Thermodynamic and circulation characteristics of winter monsoon tropical mesoscale convection. *Mon. Wea. Rev.*, **110**, 1898-1911.

Johnson, R.W., 1986: Lower-tropospheric warming and drying in tropical mesoscale convective systems: Implication for the problem of cumulus parameterization. *J. Meteor. Soc. Japan*, **64**, 721-726.

Klemp, J.B., R.B. Wilhelmson and P.S. Ray, 1981: Observed and numerically simulated structure of a mature supercell thunderstorm. *J. Atmos. Sci.*, **38**, 1558-1580.

Knupp, K.R., 1985: Precipitating convective cloud downdraft structure: A synthesis of observations and modeling. Ph.D. dissertation, Department of Atmospheric Science, Colorado State University, Fort Collins, Colorado.

Leary, C.A. and E.N. Rappaport, 1987: The life cycle and internal structure of a mesoscale convective complex. *Mon. Wea. Rev.*, **115**, 1503-1527.

Lo, C.S., W.R. Barchet and D. Martin, 1982: Vertical mass transport in cumulonimbus clouds on Day 261 of GATE. *Mon. Wea. Rev.*, **110**, 1994-2004.

Lopez, P.E., D.O. Blanchard, R. Daniel, W.L. Hiscox and M.J. Casey, 1984a: Population characteristics, development processes and structure of radar echoes in south Florida. *Mon. Wea. Rev.*, **112**, 56-75.

Mahrer, Y. and R.A. Pielke, 1976: Numerical simulation of the air flow over Barbados. *Mon. Wea. Rev.*, **104**, 1392-1402.

Mahrer, Y. and R.A. Pielke, 1977: A numerical study of the air flow over irregular terrain. *Contrib. Atmos. Phys.*, **50**, 98-113.

Mahrer, Y. and R.A. Pielke, 1978: A test of an upstream spline interpolation technique for the advective terms in a numerical mesoscale model. *Mon. Wea. Rev.*, **106**, 1758.

McNider, R.T. and R.A. Pielke, 1981: Diurnal boundary-layer development over sloping terrain. *J. Atmos. Sci.*, **38**, 2198-2212.

Ogura, Y. and M.T. Liou, 1980: The structure of a mid-latitude squall line: A case study. *J. Atmos. Sci.*, **37**, 553-567.

Pielke, R.A., 1974: A three-dimensional numerical model of the sea breeze over south Florida. *Mon. Wea. Rev.*, **102**, 115-139.

Pielke, R.A., 1984: *Mesoscale Meteorological Modeling.* Academic Press, New York, N.Y., 612 pp.

Pielke, R.A. and Y. Mahrer, 1975: Techniques to represent the heated planetary boundary layer in mesoscale models with coarse vertical resolution. *J. Atmos. Sci.*, **32**, 2288-2308.

Pielke, R.A. and Y. Mahrer, 1978: Verification analysis of the University of Virginia three-dimensional mesoscale model prediction over south Florida for 1 July 1973. *Mon. Wea. Rev.*, **106**, 1568-1569.

Purdom, J.F.W., 1976: Some uses of high resolution GOES imagery on the mesoscale forecasting of convection and its behavior. *Mon. Wea. Rev.*, **104**, 1474-1483.

Simpson, J., N.E. Westcott, R.J. Clerman and R.A. Pielke, 1980: On cumulus mergers. *Arch. Meteor. Geophys. Bioklim. Ser.*, **A.29**, 1-40.

Song, J.L., 1986: A numerical investigation of Florida's sea breeze-cumulonimbus interactions. Ph.D. dissertation, Department of Atmospheric Science, Colorado State University, Fort Collins, Colorado, 187 pp.

Song, J.L. and W.M. Frank, 1983: Relationships between deep convection and large-sale processes during GATE. *Mon. Wea. Rev.*, **111**, 2145-2160.

Song, J.L., R.A. Pielke and M. Segal, 1985: Vectorizing a mesoscale meteorological model on the CYBER 205. *Environmental Software*, January 1986.

Song, J.L. and R.A. Pielke, 1987: The influence of deep cumulus convection on sea breeze dynamics over south Florida. Part II: Model application. Atmos. Sci. Paper #427, Department of Atmospheric Science, Colorado State University, Fort Collins, Colorado.

Ulanski, S.L. and M. Garstang, 1978: The role of surface divergence and vorticity in the lifecycle of convective rainfall. Part I: Observation and analysis. *J. Atmos. Sci.*, **35**, 1047-1062.

Watson, A.I. and D.O. Blanchard, 1984: The relationship between total area divergence and convective precipitation in south Florida. *Mon. Wea. Rev.*, **112**, 673-685.

Zhang, D.L., 1985: Nested-grid simulation of the meso-β scale structure and evolution of the Johnstown flood of July 1977. Ph.D. dissertation, Pennsylvania State University, 270 pp.

Zipser, E.J., 1977: Mesoscale and convective scale downdrafts as distinct components of squall line structure. *Mon. Wea. Rev.*, **105**, 1568-1589.

At a Grid

(1) Potential Buoyant Energy — No → **EXIT** No Cloud Effect is Generated

Yes ↓

(2) STAGE I — Yes / No

Yes → Initial Grid-Scale Forcing — No
No ← Updated Forcing — No

EXIT

Yes (left) / Yes (right)

(3) "Deep" Convection — No → **EXIT**

Yes ↓

(4) Updraft Properties $\left(\dfrac{\partial \phi}{\partial t}\right)^{1}_{U}$

(5) Downdraft Properties $\left(\dfrac{\partial \phi}{\partial t}\right)^{1}_{D}$

(6) Grid-Environment Responses $\left(\dfrac{\partial \phi}{\partial t}\right)^{1}_{E}$

(7) **Grid Adjustment**
$$\left(\frac{\partial \phi}{\partial t}\right)^{1} \leftarrow \left[\left(\frac{\partial \phi}{\partial t}\right)^{1}_{U_{;}} \left(\frac{\partial \phi}{\partial t}\right)^{1}_{D_{;}} \left(\frac{\partial \phi}{\partial t}\right)^{1}_{E}\right]$$
$\phi = T, q$

STAGE I — Yes / No

(8) **RETURN** $\left(\dfrac{\partial \phi}{\partial t}\right)^{1}_{;} \phi = T, q$

$\rightarrow$ NEXT GRID

(9) **Convective Enhancement**
$$\left(\frac{\partial \phi}{\partial t}\right)^{2}_{U} = \left(\frac{\partial \phi}{\partial t}\right)^{1}_{U} * RATIO$$
$$\left(\frac{\partial \phi}{\partial t}\right)^{2}_{D} = \left(\frac{\partial \phi}{\partial t}\right)^{1}_{D} * RATIO$$
$$\left(\frac{\partial \phi}{\partial t}\right)^{2}_{E} = \left(\frac{\partial \phi}{\partial t}\right)^{1}_{E} * RATIO$$
$$RATIO = \left.\frac{(\overline{M})^{2} + |M_{D}|^{2}}{(\overline{M})^{2}}\right|_{LCL}$$

(10) **Convective Grid Adjustment**
$$\left(\frac{\partial \phi}{\partial t}\right)^{2} \leftarrow \left[\left(\frac{\partial \phi}{\partial t}\right)^{2}_{U_{;}} \left(\frac{\partial \phi}{\partial t}\right)^{2}_{D_{;}} \left(\frac{\partial \phi}{\partial t}\right)^{2}_{E}\right]$$
$\phi = T, q$

RETURN $\left(\dfrac{\partial \phi}{\partial t}\right)^{2}_{;} \phi = T, q$

NEXT GRID ←

Note: Superscript 1 = stage 1 (developing), 2 = stage 2 (mature)

Figure 1 - A schematic illustration of the cumulus parameterization derived in this study. Steps are explained in the text. The brackets in Steps (7) and (10) indicate the weighted-averaging defined in Eqs. 4 and 5.
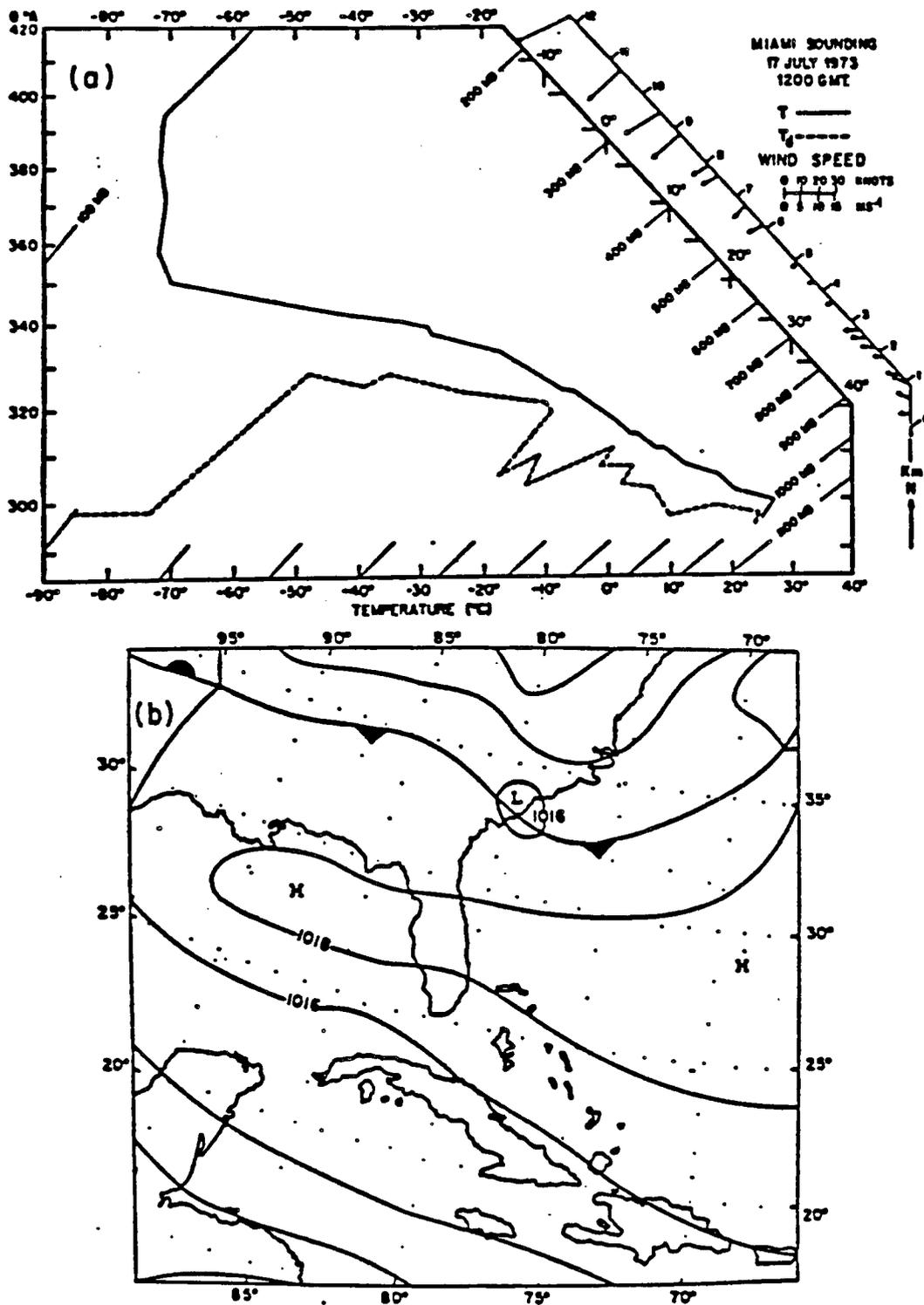
Figure 2 - The early morning (07 EST) Miami sounding (a) of 17 July 1973, which is used for initiating the moist sea breeze simulation (or the control run). The synoptic-scale surface pressure pattern over Florida region (b) at 7 a.m., 17 July 1973. The surface wind (at a speed about 4 m/s; in the direction of east-southeasterly) is used for the surface wind initiation of the control run.
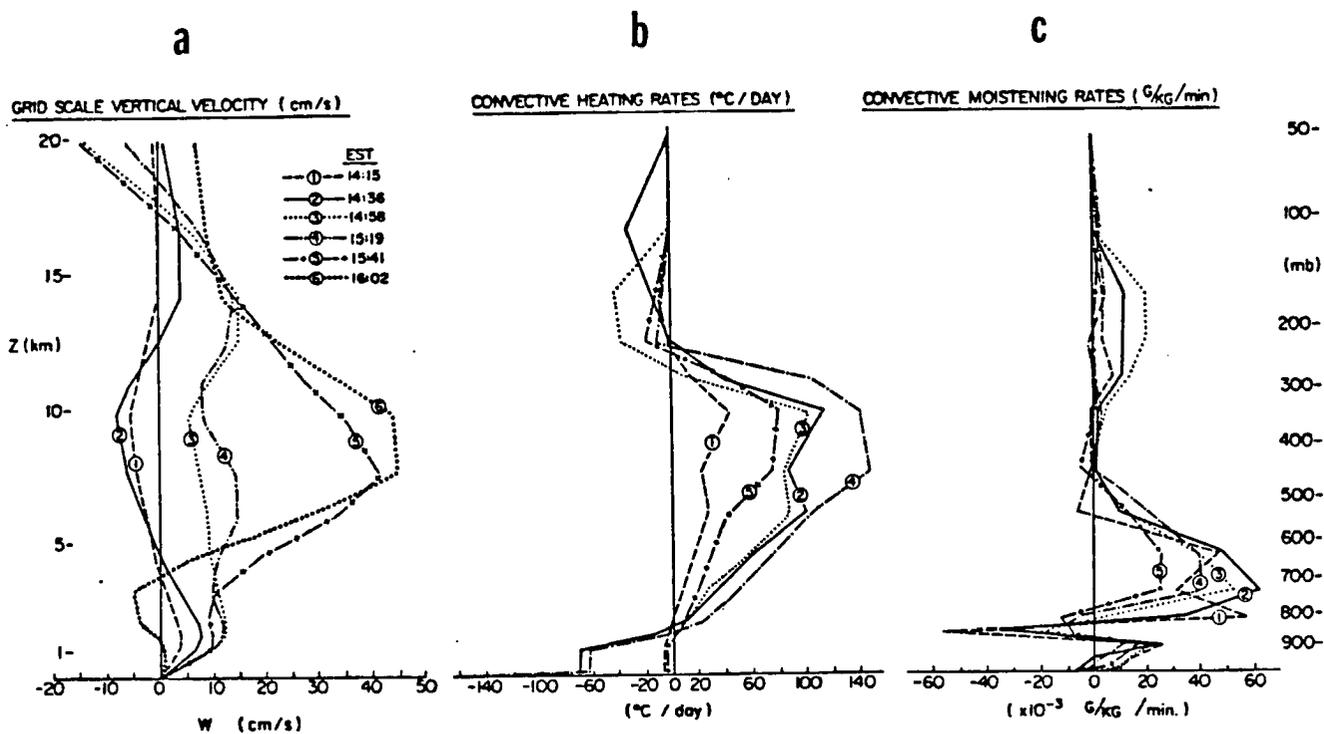
Figure 3 - (a) Grid-scale vertical velocity (cm/s) profiles at the indicated times during the control run; (b) same as Fig. 3a but for the convectively-produced heating profile obtained from the parameterization; and (c) same as Fig. 3b but for the moistening profile.

34

UPDRAFT MASSFLUX (.g/s)
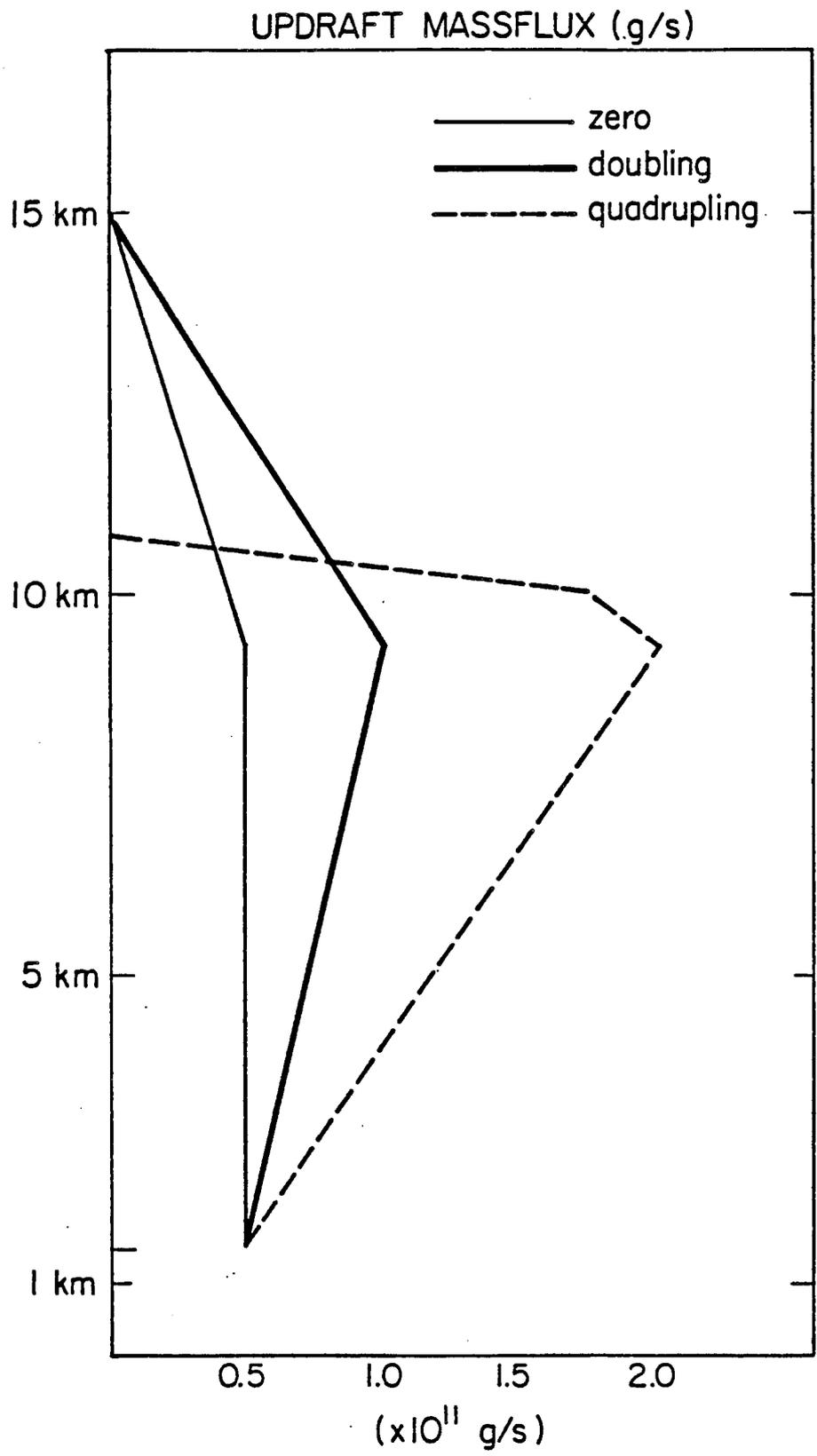
Figure 4 - Updraft mass flux profiles for the zero-entrainment (thin solid), doubling (thick solid) and the quadrupling (dashed) cases in the 1D diagnostic sensitivity tests discussed in Section 3.
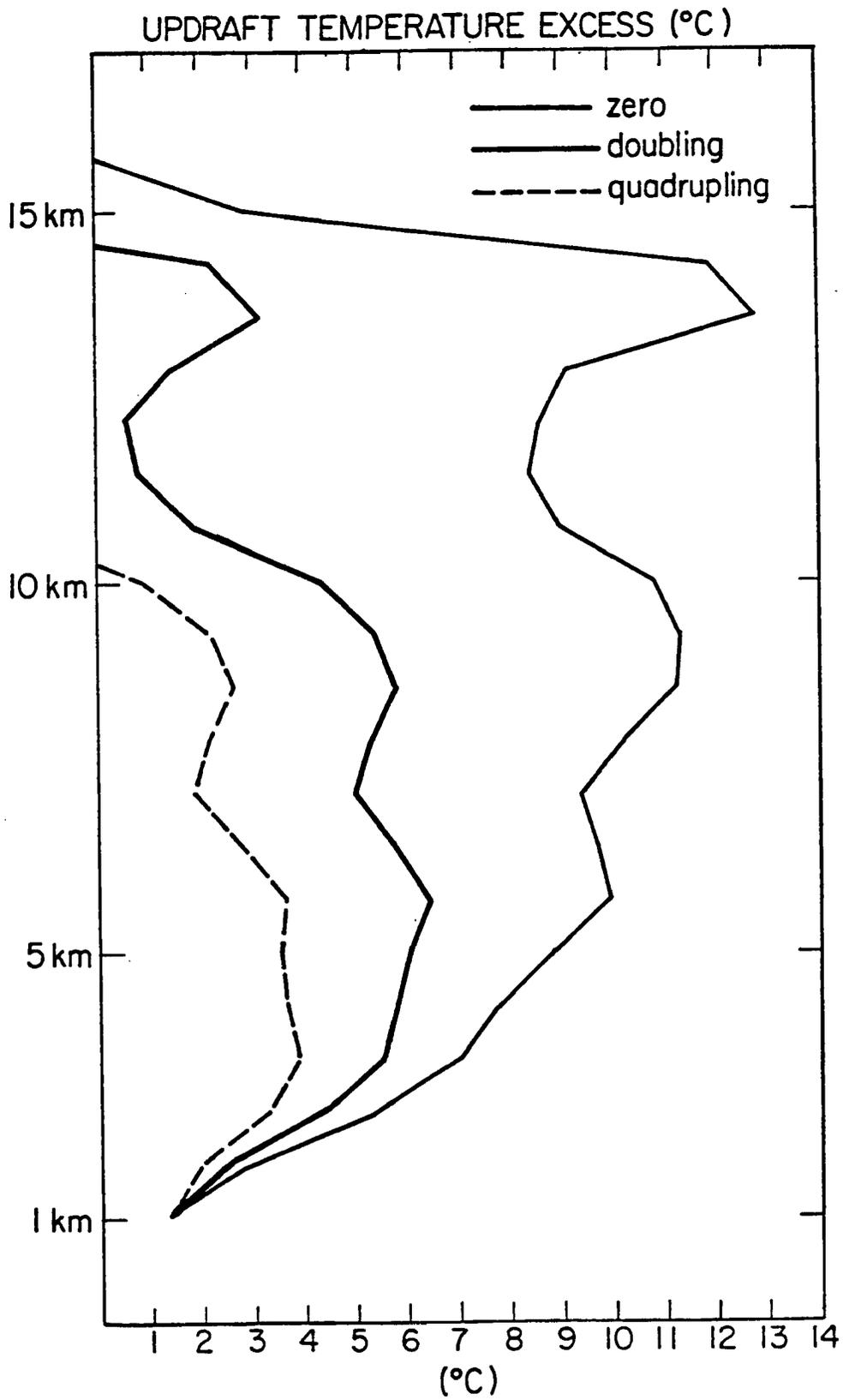
Figure 5 - Same as Fig. 4 but for the updraft temperature-excess profiles.
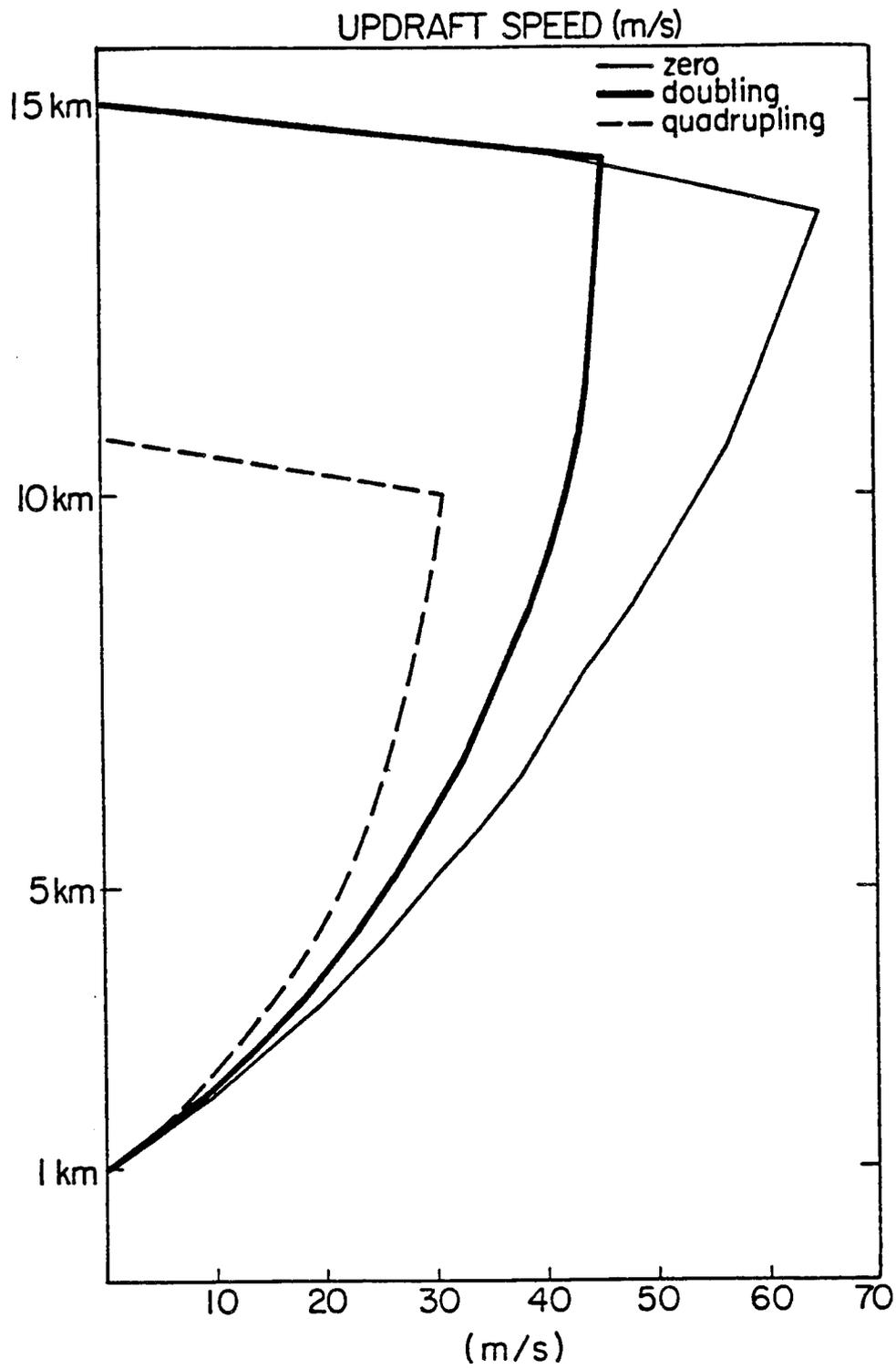
Figure 6 - Same as Fig. 4 but for updraft speed profiles.
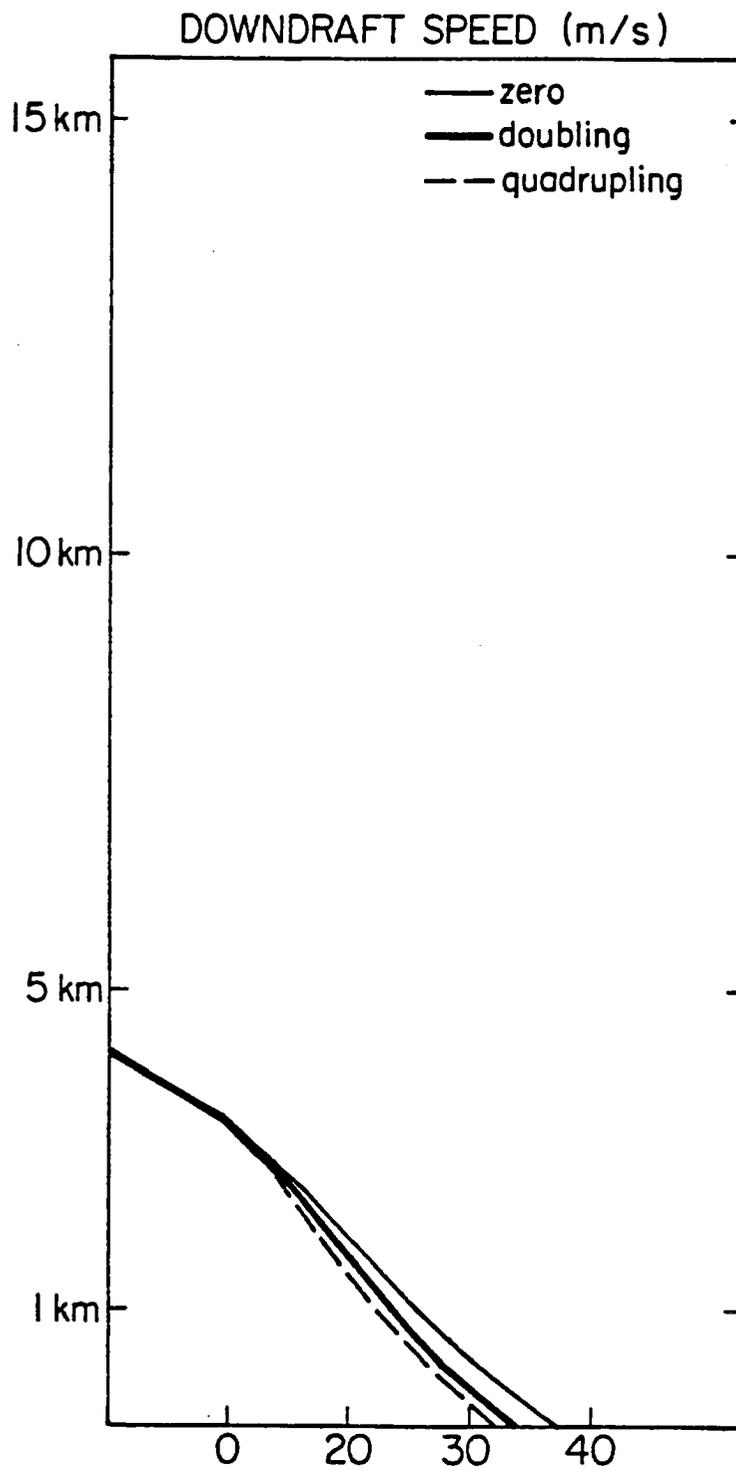
Figure 7 - Same as Fig. 4 but for downdraft speed profiles.
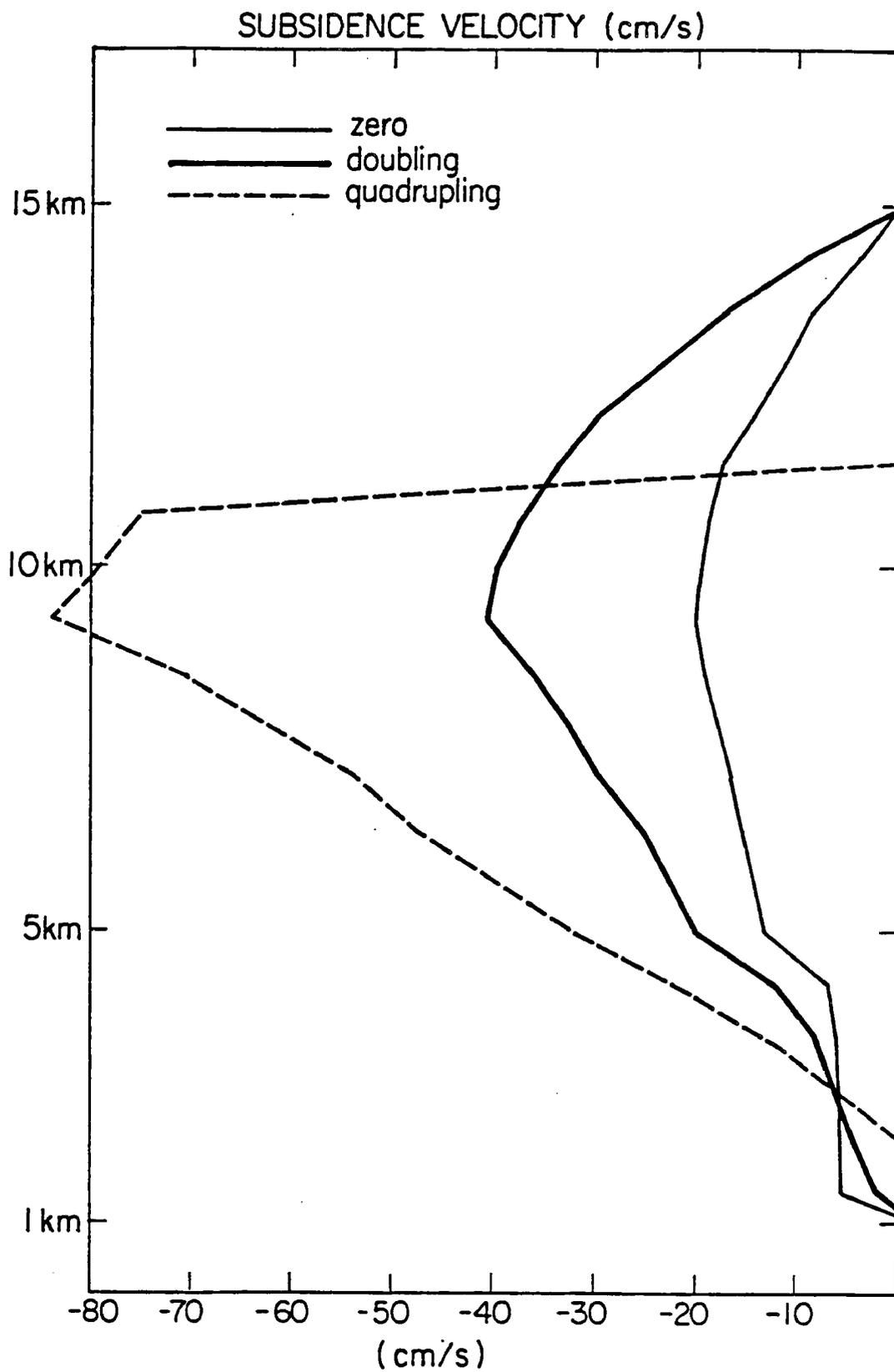
Figure 8 - Same as Fig. 4 but for the grid-environmental subsidence velocity profiles.
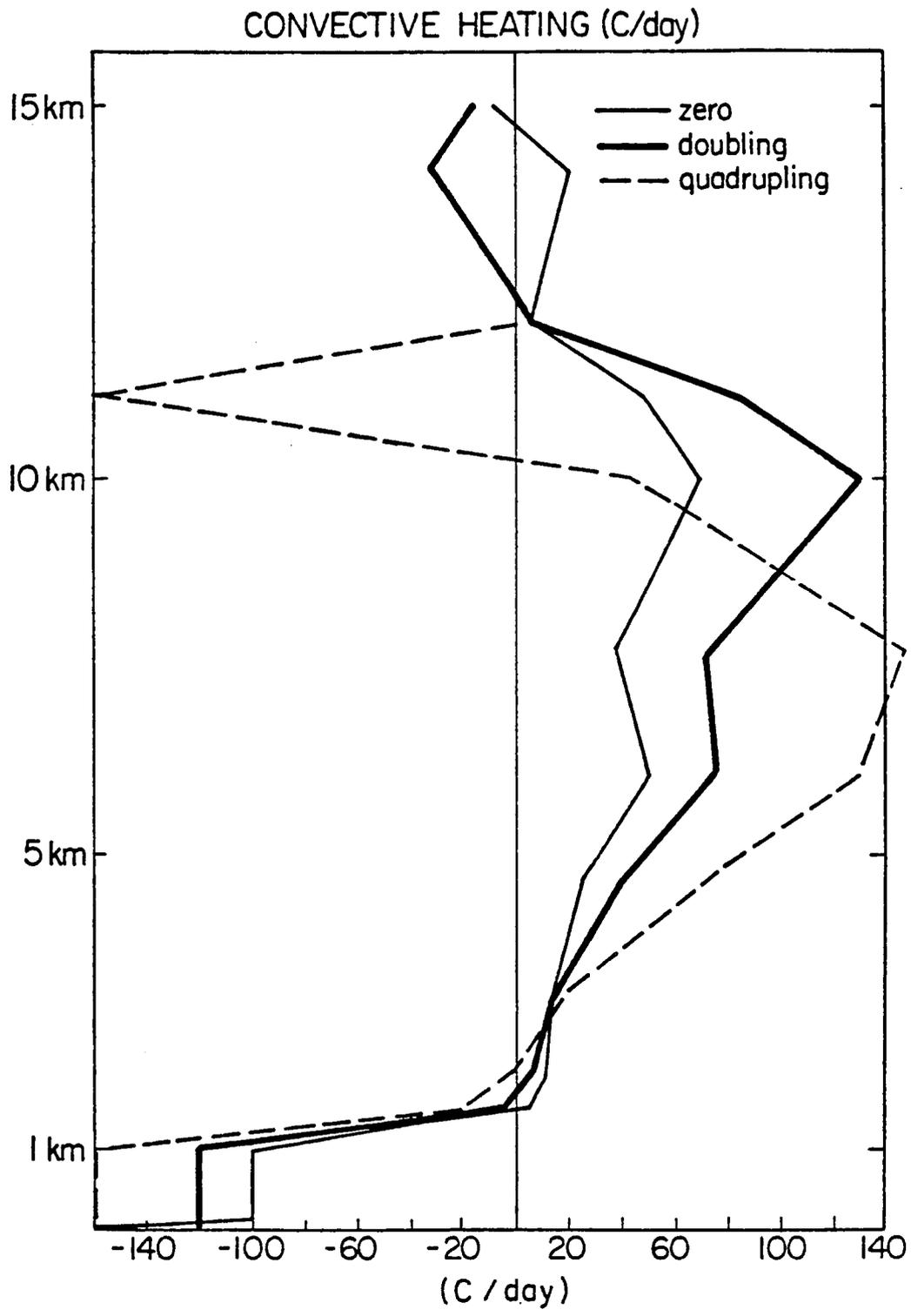
Figure 9 - Same as Fig. 4 but for the convectively-produced heating profiles obtained from the parameterization.
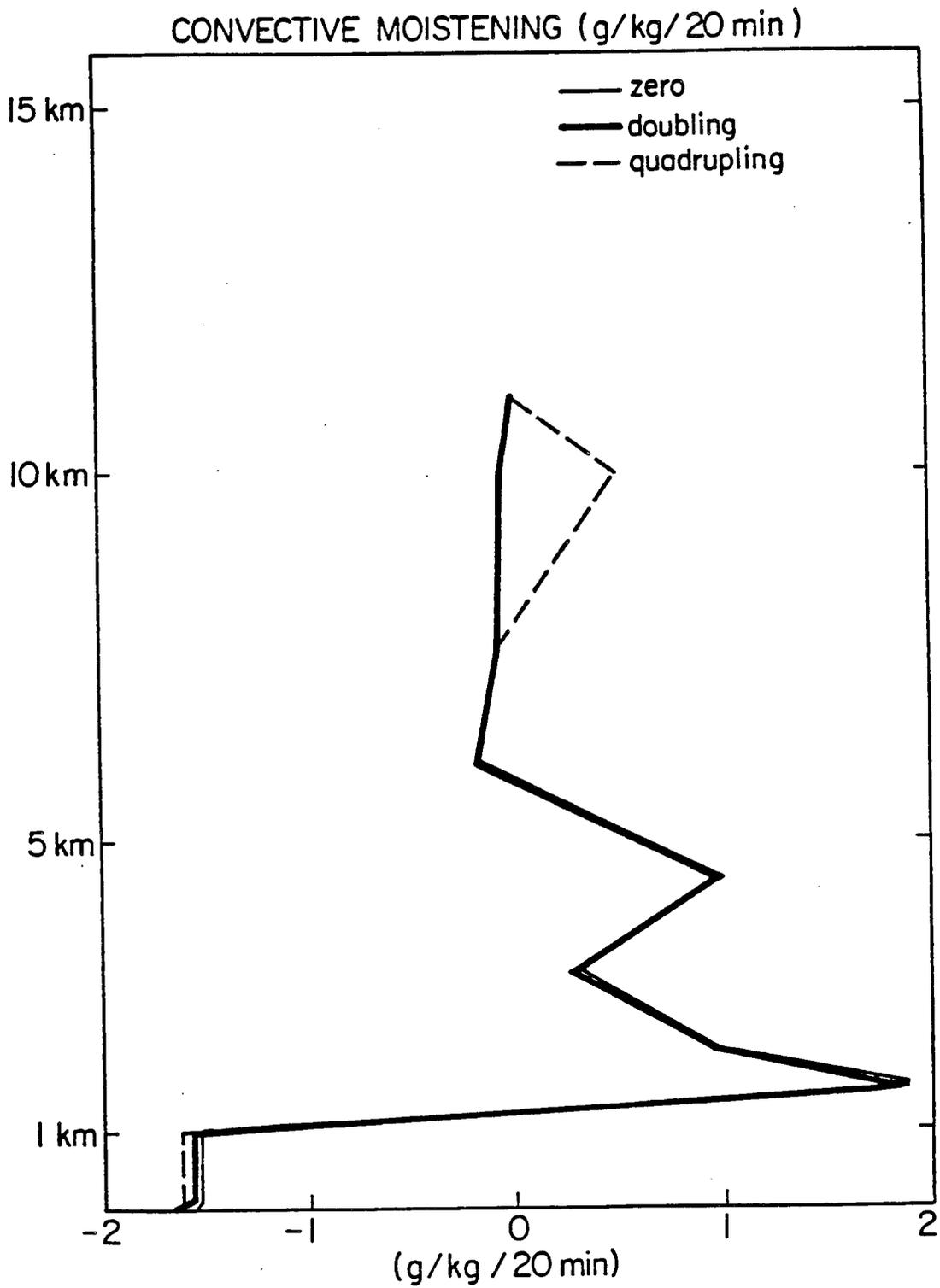
Figure 10 - Same as Fig. 4 but for the convectively-produced moistening profiles obtained from the parameterization.

PEF	Total rainfall (g/s)	(mm/hr)	ΔTD_{ML}*	Anvil-Evaporational cooling (°C)	moistening (g/kg)
10%	0.81×10^8	~0.8	-2.97	-2.02	+0.0954
30%	0.24×10^9	~2.3	-3.25	-2.01	+0.0691
50%	0.41×10^9	~4.0	-3.54	-1.94	+0.0428
70%	0.57×10^9	~6.0	-3.82	-0.45	+0.0164
90%	0.73×10^9	~8.0	-4.10	-0.08	-0.0099

* ΔTD_{ML}: Downdraft temperature-deficit in the melting layer.

Table 3-1 - Sensitivity of the selected parameterization results due to changing the pre-specified constant precipitation efficiency. The downdraft temperature-deficit is defined as subtracting the virtual potential temperature of the grid-environment from that of the downdraft.

α	Downdraft surface max. temperature deficit (°C)	Max. cooling at surface (°C)
10%	-11.82	-5.20
30%	-12.34	-5.39
50%	-12.80	-5.56
70%	-13.40	-5.79
90%	-13.99	-6.02

Table 3-2 - Same as Table 3-1 but for changing the parameter associated with the downdraft initial thermodynamic property. The final cooling (right-most column) is obtained from the weighted averaging which includes the downdraft contribution (center column).

ε	Downdraft massflux at cloud base (g/s)	Fraction of surface grid area of the downdraft replacement (%)	Max. final cooling (°C)	surface-layer drying (g/kg)
10%	0.85×10^{10}	14.3	-1.89	-0.024
30%	0.26×10^{11}	33.3	-4.41	-0.057
50%	0.43×10^{11}	45.5	-6.02	-0.078
70%	0.60×10^{11}	53.8	-7.13	-0.092
90%	0.77×10^{11}	60.0	-7.94	-0.103

Table 3-3 - Same as Table 3-2 but for changing the parameter associated with the downdraft initial mass flux.

RHD	Downdraft evaporation (g/s)	Max. surface temperature deficit (°C)[**]	Max. surface[**] cooling (°C)	drying (g/kg)
70%	0.17×10^9	-11.11	-4.63	-0.102
90%	0.22×10^9	-13.99	-6.02	-0.078

[**]The surface cooling is the surface temperature deficit times the fraction of grid area associated with the surface-layer downdraft replacement.

Table 3-4 - Same as Table 3-2 but for changing the pre-specified constant downdraft relative humidity.

- Horizontal Momentum Equations

$$\frac{\partial \bar{u}}{\partial t} = -\bar{v}_2 \cdot \nabla \bar{u} - \bar{w}\frac{\partial \bar{u}}{\partial z} + f\bar{v} - fV_g - \bar{\theta}\frac{\partial \bar{\pi}}{\partial x} + \frac{\partial}{\partial z}\left[K_z^m \frac{\partial \bar{u}}{\partial z}\right] + H_u$$

$$\frac{\partial \bar{v}}{\partial t} = -\bar{v}_2 \cdot \nabla \bar{v} - \bar{w}\frac{\partial \bar{v}}{\partial z} - f\bar{u} + fU_g - \bar{\theta}\frac{\partial \bar{\pi}}{\partial y} + \frac{\partial}{\partial z}\left[K_z^m \frac{\partial \bar{v}}{\partial z}\right] + H_v$$

- Thermodynamic Energy Equation

$$\frac{\partial \bar{\theta}}{\partial t} = -\bar{v}_2 \cdot \nabla \bar{\theta} - \bar{w}\frac{\partial \bar{\theta}}{\partial z} + \frac{\partial}{\partial z}\left[K_z^\theta \frac{\partial \bar{\theta}}{\partial z}\right] + H_\theta + \frac{\delta \bar{\theta}}{\delta t}\bigg|_R + \frac{\delta \bar{\theta}}{\delta t}\bigg|_C$$

- Moisture Conservation Equation

$$\frac{\partial \bar{q}}{\partial t} = -\bar{v}_2 \cdot \nabla \bar{q} - \bar{w}\frac{\partial \bar{q}}{\partial z} + \frac{\partial}{\partial z}\left[K_z^q \frac{\partial \bar{q}}{\partial z}\right] + H_q + \frac{\delta \bar{q}}{\delta t}\bigg|_C$$

- Deep Continuity Equation

$$\nabla_3 \cdot \rho_o \bar{v}_3 = 0$$

$$\bar{w}_j = \frac{\rho_{o_{j-1}}}{\rho_{o_j}}\bar{w}_{j-1} + \frac{.5*(\rho_{o_j}+\rho_{o_{j-1}})}{\rho_{o_j}}(-\nabla\cdot\bar{v}_2) \cdot (z_j - z_{j-1})$$

- Model Top Height Equation

$$\Delta S = \left[\bar{w}_{top} - \bar{u}\frac{\partial S}{\partial x} - \bar{v}\frac{\partial S}{\partial y}\right]\Delta t$$

- Diagnostic Hydrostatic Pressure Equation

$$\bar{\pi}_{top}^\tau = \bar{\pi}_{top}^{\tau-1} - \Delta S\frac{g}{\bar{\theta}_{top}}$$

$$\bar{\pi}_j = \bar{\pi}_{j+1} + g \cdot \int_j^{j+1}\frac{1}{\bar{\theta}}dz \quad , \quad \bar{\pi} = C_p\left(\frac{\bar{p}}{P_{oo}}\right)^{R_d/C_p}$$

Appendix A-1 - Governing equations of the mesoscale model.

Symbol	Definition
$\bar{u}, \bar{v}, \bar{w}$:	Grid-Volume-Averaged (GVA) velocity components in the Cartesian x,y,z coordinates, respectively.
$\bar{\theta}, \bar{q}, \bar{p}, \bar{\pi}$:	The GVA quantities of, respectively, potential temperature, specific humidity, pressure, and scaled-pressure (Figure 1).
V_g, U_g :	Geostrophic wind components.
K_z^m, K_z^θ, K_z^q:	Turbulent vertical exchange coefficients of, respectively, horizontal momentum, potential temperature and specific humidity.
H_u, H_v, H_θ, H_q:	Horizontal filter effects on, respectively, the u and v velocity components, potential temperature and specific humidity.
$\left.\dfrac{\delta\bar{\theta}}{\delta t}\right\|_R$:	Radiation effects on the potential temperature.
$\left.\dfrac{\delta\bar{\theta}}{\delta t}\right\|_C, \left.\dfrac{\delta\bar{q}}{\delta t}\right\|_C$:	Deep convective effects on the potential temperature and specific humidity.
$\bar{v}_2, \bar{v}_3$:	The GVA 2D (horizontal) and 3D wind vectors.
∇, ∇_3 :	Horizontal and 3D del-operators.
ρ_o :	Synoptic density (a function of height only).
S :	Model top height
j, τ :	Index of, respectively, model vertical levels and time steps.
R_d :	Dry gas constant.
C_p :	Specific heat at constant pressure.
P_{oo} . :	Reference pressure (1000 mb).
g :	Gravitation constant.
f :	Coriolis parameter.

Appendix A-2 - Symbols used in the paper.

z (cm)	$\frac{\delta T}{\delta t}$ ($\frac{°C}{20\ min}$)	$\frac{\delta T}{\delta t}$ ($\frac{°C}{day}$)	$\frac{\delta q}{\delta t}$ ($\frac{g/g}{s}$)	$\frac{\delta q}{\delta t}$ ($\frac{g/kg}{20\ min}$)	θ_{new}	θ_{old}	q_{new}	q_{old}
2072839.0	-.00	-.00	-.0000000	-.0000000	476.00	476.00	.0000100	.0000100
1662468.0	-.22	-16.00	.0000000	.0000001	367.06	367.28	.0000100	.0000100
1421823.0	-.53	-38.07	.0001360	.0067996	337.79	338.32	.0001461	.0000101
1243921.0	.10	7.21	.0000020	.0000996	335.41	335.31	.0000120	.0000100
1096781.0	1.14	82.26	.0000956	.0047802	333.23	332.08	.0001114	.0000158
970418.0	1.64	118.42	-.0000510	-.0024584	330.70	329.06	.0002987	.0003497
760291.0	.74	53.01	-.0000649	-.0032467	323.76	323.02	.0014321	.0014970
589461.0	.82	59.01	-.0001570	-.0078493	316.34	315.52	.0034210	.0035780
589461.0	.82	59.01	-.0001570	-.0078493	316.34	315.42	.0034210	.0035780
445078.0	.42	30.17	.0009492	.0474582	310.36	309.94	.0044862	.0035370
319663.0	.17	12.33	.0004383	.0219167	305.38	305.20	.0076903	.0072520
208384.0	-.00	-.33	.0014895	.0744775	303.80	303.80	.0101235	.0086340
156975.0	-.11	-7.64	-.0003296	-.0164816	302.35	302.45	.0135404	.0138700
108086.0	-.67	-48.17	-.0001843	-.0092135	301.96	302.63	.0157857	.0159700
61351.0	-.67	-48.17	-.0005943	-.0297135	301.96	302.63	.0157857	.0163800
16487.0	-.67	-48.17	-.0008043	-.0402135	301.96	302.63	.0157857	.0165900
1718.0	-2.09	-150.57	-.0003449	-.0172467	302.61	304.71	.0163851	.0167300

Appendix B-1 - Parameterization results without performing the adjustment of requiring the conservations of both moist static energy and water substance.

z (cm)	$\frac{\delta T}{\delta t}$ ($\frac{°C}{20\ min}$)	$\frac{\delta T}{\delta t}$ ($\frac{°C}{day}$)	$\frac{\delta q}{\delta t}$ ($\frac{g/g}{s}$)	$\frac{\delta q}{\delta t}$ ($\frac{g/kg}{20\ min}$)	θ_{new}	θ_{old}	q_{new}	q_{old}
2072839.0	-.01	-.60	-.0000000	-.0000000	475.99	476.00	.0000100	.0000100
1662468.0	-.23	-16.46	-.0000000	-.0000000	367.06	367.28	.0000100	.0000100
1421823.0	-.53	-38.39	.0001031	.0051568	337.79	338.32	.0001132	.0000101
1243921.0	.09	6.83	.0000019	.0000940	335.40	335.31	.0000119	.0000100
1096781.0	1.14	81.90	.0000952	.0047594	333.22	332.08	.0001110	.0000158
970418.0	1.64	118.07	-.0000571	-.9925844	330.70	329.06	.0002980	.0003497
760291.0	.73	52.69	-.0000669	-.0033432	323.75	323.02	.0014301	.0014970
589461.0	.82	58.71	-.0001616	-.0080795	316.33	315.52	.0034164	.0035780
445078.0	.42	29.89	.0009284	.0464198	310.35	309.94	.0044654	.0035370
319663.0	.17	12.06	.0003888	.0194398	305.37	305.20	.0076408	.0072520
319663.0	.17	12.06	.0003888	.0194398	305.37	305.20	.0076408	.0072520
208384.0	-.01	-.60	.0014065	.0703240	303.79	303.80	.0100405	.0086340
156975.0	-.11	-7.91	-.0003777	-.0188827	302.34	302.45	.0134923	.0138700
108086.0	-.67	-48.36	-.0002260	-.0112987	301.96	302.63	.0157440	.0159700
61351.0	-.67	-48.36	-.0006360	-.0317987	301.96	302.63	.0157440	.0163800
16487.0	-.67	-48.36	-.0008460	-.0422987	301.96	302.63	.0157440	.0165900
1718.0	-2.09	-150.57	-.0004506	-.0225320	302.61	304.71	.0162794	.0167300

Appendix B-2 - Same as Appendix B-1 but <u>with</u> the adjustment.

The Influence of Deep Cumulus Convection on Sea Breeze Dynamics Over South Florida Part II: Model Application

by

J.L. Song and R.A. Pielke

Department of Atmospheric Science
Colorado State University
Fort Collins, Colorado

Colorado
State
University

Department of
Atmospheric Science

The Influence of Deep Cumulus Convection on Sea Breeze Dynamics Over South Florida Part II: Model Application

by

J.L. Song and R.A. Pielke
Department of Atmospheric Science
Colorado State University
Fort Collins, Colorado 80523

Atmospheric Science Paper No. 427

May 16, 1988

Table of Contents

List of Figures

Figure 9 - Horizontal distributions at 9 m of model produced horizontal divergences at 1 p.m. (1300 EST). (10^{-4} s^{-1}) from the control run (indicated as "total") (top); and from the difference by subtracting a dry run result from the control run result (indicated as "total-dry" (bottom). "H" indicates divergence center and "L" indicates convergence center.

Figure 10 - Same as Fig. 9 but for 2 p.m. (1400 EST).

Figure 11 - Same as Fig. 9 but for 3 p.m. (1500 EST).

Figure 12 - Same as Fig. 5 but for 4 p.m. (1600 EST).

Figure 13 - Same as Fig. 6 but for 4 p.m. (1600 EST).

Figure 14 - Same as Fig. 5 but for 5 p.m. (1700 EST).

Figure 15 - Same as Fig. 6 but for 5 p.m. (1700 EST).

Figure 16 - The "total-dry" potential temperature (K$^\circ$, top) and horizontal divergence (10^{-4} s^{-1}, bottom) at 1500 EST, on the XZ-cross section indicated by the AB line in Fig. 11. The two coasts are indicated by the short vertical lines with "W" and "E" marks, respectively, shown on the bottoms of the XZ-cross section.

Figure 17 - Same as Fig. 16 but for horizontal u-velocity (m/s, top) and Y-direction vorticity (10^{-4} s^{-1}, bottom). For the letter, positive values correspond to clockwise rotation on the XZ-plane.

Figure 18 - Same as Fig. 16 but for vertical velocity (cm/s, top) and vertical vorticity (10^{-4} s^{-1}, bottom).

Figure 19 - Same as Fig. 16 but for 4 p.m. (1600 EST).

Figure 20 - Same as Fig. 17 but for 4 p.m. (1600 EST).

Figure 21 - Same as Fig. 18 but for 4 p.m. (1600 EST).

Figure 22 - Profiles of model horizontal divergence (left) and vertical vorticity (right) averaged over an area about 350 km x 350 km, at the three times indicated and for the three sensitivity simulations discussed in Section 4.2.

Figure 23 - Vertical grid-scale moisture fluxes (wq) at 1500 EST (top) and 1600 EST (bottom) on the XZ-cross section shown by the AB line in Fig. 11. The vertical velocity

(w) is in cm/s, while model's specific humidity (q) is in kg/kg. The magnitudes shown in the figures are for the products wq.

Figure 24 - The conceptual model for the Stage-1, or the sea breeze convergence stage, of the convective-environmental interaction over southern Florida (on the XZ-cross section shown by the AB line in Fig. 11) during synoptically undisturbed days. Main points shown in this figure include: (1) embedded deep cumulus convection within the sea breeze convergence zone, (2) a vertically stretched solenoidal circulation, (3) divergence and vorticity maxima coincide, and (4) the convective downdraft cooling effect is not yet significant.

Figure 25 - The Stage-1 horizontal divergence 10^{-4} s^{-1}, top) and vertical vorticity (10^{-4} s^{-1}, bottom) at 9 m.

Figure 26 - Same as Fig. 24 but for the Stage-2, or the convective downdraft cooling stage. Main points shown in this figure include: (1) an upwind propagation, (2) mid-tropospheric convergence, (3) a "four-cell" vertical circulation pattern, (4) mesoscale upward and downward motions, and (5) a phase shift between divergence and vorticity maxima.

Figure 27 - Same as Fig. 25 but for the Stage-2.

Figure 28 - Same as Fig. 24 but for the Stage-3, or the decaying stage. Main points shown in this figure include: (1) mesoscale weaker upward and downward motions, (2) a decaying sea breeze, (3) lower-tropospheric drying, and (4) surface convergence farther away from deep convection.

Abstract

Mesoscale - Convective interactions in Florida's sea breeze environment are investigated using a numerical approach with supportive observations. The numerical tools, including a hydrostatic primitive-equation model (Pielke, 1974) and a newly derived cumulus parameterization, are introduced in the accompanying paper (Song and Pielke, 1987).

Numerical results show that the continuous sea breeze-deep convective interaction is the most important necessary condition for maintaining the Florida summertime deep convection. Mesoscale responses due to deep convective forcing during the convectively mature stage are such that a "four-cell" solenoidal circulation is produced, as distinguished from a "two-cell" solenoidal circulation during the earlier stage of the system. Significant thermodynamic asymmetry over a mesoscale area is found in the mid and lower troposphere during the mature stage of the system. Associated with this asymmetry are two air streams: a moist front-to-rear jet (MFJ) originating in the moist planetary boundary layer; and a dry rear-to-front jet (DRJ) originating in the mid-troposphere. Steady-state mesoscale convection would occur with a balance between the MFJ and the DRJ. The loss of such a balance would indicate either a further enhanced convective development (i.e., if the MFJ dominates) or a decaying stage (i.e., if the DRJ dominates).

1 Introduction

Sea breezes have been intensively observed (e.g, Hsu, 1969) and modeled (e.g., Pielke, 1974) for at least the last twenty years. A review of many of the investigations is presented in Pielke (1984, pgs. 456-464). As a result of these studies, a relatively clear understanding of the relation of the sea breeze to thunderstorm initiation and maintenance has been achieved. However, as indicated in the accompanying paper (Song and Pielke, 1987, hereafter referred to as Part I), there has not been documented thus far in the literature the peninsula-scale sea breeze-convective interaction investigation over a time period corresponding to the lifetime of the sea breeze circulation. Such a task is undertaken in the present study. The numerical technique was introduced in Part I, in which a convective parameterization was illustrated, together with one-dimensional sensitivity tests and a brief description of how the parameterized deep convective feedback effects are incorporated into the mesoscale prognostic model.

In the current paper, the observed Florida summertime convective activities are first illustrated using a recent satellite data analysis performed by McQueen and Pielke (1985). Model results are then compared with the observations reported in Pielke and Cotton (1977), Burpee and Lahiff (1984), McQueen and Pielke (1985), and Michaels *et al.* (1987). Following the model verificational analysis, the sea breeze-convective interactions over south Florida will be discussed in four subtopics, namely (a) mesoscale tropospheric circulation patterns in response to deep convection; (b) peninsula-scale (horizontally averaged) forcing and its relation to the coastal deep convection; (c) mid/low tropospheric mesoscale air flows which are associated with the mature stage of convection; and (d) conceptual models of the distinct stages during the lifetime of the sea breeze-convective interaction.

1

2 An Observational Analysis

As described in McQueen and Pielke (1985), geostationary satellite imagery (summer, 1983) was analyzed for 34 days at two-hour intervals and composited using a classification which defines strong geostrophic flow as greater than 3.5 ms^{-1}, and light and variable flow as less than 1 ms^{-1}. Regions of deep cumulus convection were identified as regions of bright clouds, determined quantitatively from the visible 0.8 km resolution images, and with cold tops, defined as less than $-38°C$, as evaluated from the infrared 13 km resolution imagery (a more detailed description of the analysis is presented in McQueen and Pielke, 1985). The percentage of coverage of land and of water by deep cumulus convection was evaluated as a function of time of day as shown in Fig. 1. The diurnal variation in convective activity is clear in Fig. 1, with the disturbed days apparently being somewhat less dependent on solar heating. In particular, we see that the Florida deep convective activities for the relatively undisturbed days (or the sea breeze days as defined in Burpee and Lahiff, 1984) have their peak intensities around 1600 EST (2100 GMT).

Examples of the composite diurnal variation in deep convection as viewed from the satellite is illustrated for light southeast geostrophic flow and strong southeast geostrophic flow over south Florida in Figs. 2a-d for 1200, 1400, 1600, and 1800 EST, respectively. Evident in Fig. 2a, the earliest deep convective activity over southern Florida is in the southern tip of the peninsula (for both flow cases) and the west coastal area near Fort Meyers (for the light flow case, top) and to the south of Lake Okeechobee (for the strong flow case, bottom). By 1400 EST, Fig. 2b shows that the southern tip and the nearby southwest coastal area of the Florida peninsula are associated with relatively significant deep convective activities. Stronger geostrophic flow is associated with stronger convection in the eastern part of the peninsula including Lake Okeechobee, while in the light geostrophic flow situation more convective activities are seen along the west coast. By 1600 EST (Fig. 2c), relatively significant convective activities occur with both flow regimes to the west and

2

southwest of Lake Okeechobee (i.e., in the region between the lake and Fort Meyers). Other than this area (as at 1400 EST), more convection occurs along the east coast in the stronger flow case. By 1800 EST, (Fig. 2d) deep convective activity nearly vanishes for the light flow case except for the area just to the north of the lake. On the other hand in the stronger flow case widespread activities at this time occur in the northwest portion of southern Florida.

In an attempt to extend the data base of preferred locations of deep cumulus convection over Florida from that available using geostationary satellite imagery, Michaels *et al.* (1987) analyzed 10,025 hours of 47.6 x 47.6 km^2 gridcell manually digitized radar (MDR) data for June-August, 1978 through 1982, from a data tape supplied by Roy Jenne of NCAR. Deep convection is defined as a Video Integrator and Processor (VIP) brightness of 3.0 or greater (Reap and Foster, 1979).

Fig. 3 shows the mean percent in which deep convection is observed within a grid analysis area. As high as 15 percent of the total observed hours over the southwestern peninsula areas near the southern tip have deep convection activity occurring somewhere within the grid area. Fig. 4 shows the mean percentage of the corresponding about 379 days in the study in which deep convective activities are observed. As many as 84 percent of the summer (June-August) days display MDR echoes of 3.0 or greater along the southwestern coast. As indicated in Michaels *et al.* (1987), the hourly maximum in Fig. 3 is concentrated over smaller areas than the mean daily maximum percent of occurrence in Fig. 4, apparently because there are more hours of activity during many days in these high hourly average locations, but the likelihood of at least one thunderstorm during the day within a grid area is greater elsewhere in coastal southwest Florida. These figures illustrate the climatologically most favored deep convective pattern over the peninsula during summer afternoon.

3 Model Results

Model results to be shown in this section include vertical velocities near 10 km and 1 km and model generated surface rainfall maps for the time period of 1300 EST to 1700 EST at an interval of one hour. Vertical velocities are shown in units of cm s^{-1}, with a contour interval of 3 cm s^{-1}. Rainfall results shown are the convective rainfall rates (mm (hour)$^{-1}$) obtained from the parameterization and averaged in time over a 10-minute period around the hour. The model results are contrasted in this section with the climatological analyses discussed in the last section, and with the observations for the specific date corresponding to the model run. The initial surface synoptic field and thermodynamic sounding used to initialize the model were presented in Fig. 1b of Part I.

Fig. 5 shows the vertical velocity maps at 1300 EST near 10 km (top) and 1 km (middle), as well as the rainfall rate map (bottom). We see that during synoptically undisturbed days with a low-level east-southeasterly wind as represented in this simulation, the southern tip of the Florida peninsula and its nearby southwest coastal area are associated with the earliest deep convection. The northwest coastal zone of the domain (slightly south of Tampa) is associated with a secondary peak of the deep cumulus convective activity at this time. Fig. 6 shows the radar reflectivity map at surface at 1300 EST on 17 July 1973. The convective activities over the southern peninsula were associated approximately with two elongated zones: one along the southwest coast and the other extended (NNE-SSW) from the east side of Lake Okeechobee to the southwest corner of the peninsula.

Comparing the model results at 1300 EST (Fig. 5) with the radar reflectivity map (Fig. 6), we see that the model has simulated the precipitation zone around the southern tip and the nearby southwest coastal area. The radar rainfall observed to the south and immediate southeast of Lake Okeechobee is not simulated. The reason for this deficiency, in addition to the fact that a numerical model can never really exactly reproduce the real world, is that using 22 km as the horizontal grid spacing, the divergence over the lake area is not

4

well resolved resulting in the lack of convergence in the surrounding area. The coastal-area convergences, on the other hand, are well simulated because the sea breeze circulation (as contrasted to the lake breeze circulation) is adequately represented in the model. (The rationale for using a horizontal grid mesh of 22 km is to permit treatment of deep cumulus activity as entirely a subgrid scale process, as discussed in Part I.) Pielke (1974) and Pielke and Mahrer (1978) obtained substantial ascent in this area when 11 km was used as the grid spacing, in their "dry" sea-breeze simulations (i.e., no convective effects included).

Fig. 7 shows that two peak areas of model rainfall are produced by 1400 EST: one along the west coast to the north of the lake, and the other along the southwest coast. The rainfall map (Fig. 7, bottom) indicates that light rain covers a large area of the southern peninsula. The peak rainfall rates (about 17mm/hr near 1400 EST, 28 mm/hr near 1500 EST, 24 mm/hr near 1600 EST) are consistent with the observed values (about 25 mm/hr during the afternoon).

By 1500 EST, the most significant development in the simulation is the generation of a new precipitation center immediately to the west of the lake (Fig. 8, bottom) which is stronger than the two nearby centers. The latter are associated with the two peaks shown in the previous hour's map (Fig. 7). This new activity has resulted in response to the downdraft cooling produced from the earlier two convective systems. The cooling creates a horizontal pressure gradient between that region and the adjacent volume in which the air was not modified by the downdraft cooling.

In order to see how the merged convective region is generated from the previously separated convective zones, a dry sea breeze simulation was performed which is otherwise exactly the same as the moist sea breeze simulation except that no convective parameterization was included. By subtracting the results of the dry simulation from the moist simulations, we obtain the mesoscale responses due to "pure" cumulus convective forcing. In the following figures, "total" refers to the result of the moist sea breeze simulation (i.e., sea breeze

plus deep cumulus convection), while "total-dry" refers to the result due to only the deep convective effect.

Fig. 9 shows model produced surface divergence (9 m above surface) at 1300 EST for the control run (top) and for the pure convective effect (bottom). It is seen from Fig. 9 (top) that convergence at 9 m occurs throughout the peninsula except Lake Okeechobee, while surface divergence occurs over the surrounding water, with larger values just off the west coast. Since at this time the deep convective feedbacks upon its environment are not yet significant, the west coast convergence zone represents the sea breeze forcing for initiating the deep convection. The location of the west coastal sea breeze convergence zones at this time agree well with those of Pielke (1974), and Pielke and Mahrer (1978) for dry sea breeze simulations. Fig. 9 (bottom), however, indicates that deep convection is producing a dramatically different surface divergence pattern around the southern tip of the peninsula. The enhanced convergences surrounding the deep convection result from low-level wind accelerating out from the downdraft cooled boundary layer air towards the areas with an unmodified warmer boundary layer environment. Fig. 10 and 11 show, respectively, the "total" and "total-dry" surface divergence patterns at 1400 EST and 1500 EST. Three conclusions can be obtained from these figures.

(a) The coastal elongated convective zone (Fig. 11, bottom) is generated due to the combination of a merging process associated with a mesoscale circulation generated by the downdraft cool outflows from the two previously separated convective regions (Fig. 10, bottom) and the continuous sea breeze forcing.

(b) The peninsular-scale surface divergence pattern has been significantly modified locally due to the deep cumulus effects (seen by comparing Fig. 11, top with Fig. 9, top). The localized reduction of sea breeze convergences by the convective downdraft effect has been discussed by Burpee (1979), Cooper et al. (1982), among others.

6

(c) The inland propagation of the coastal convective systems is due to the combination of an inland propagation driven by the migration of the sea breeze convergence zone (Frank *et al.*, 1967) and a discrete propagation produced by downdraft cooled lower level air juxtaposed to the adjacent unmodified warm boundary layer. This inland propagation can be seen by the eastward displacement of a surface convergence center located between Lake Okeechobee and the west coast at the same latitude.

The inland propagation of the coastal convective system is more clearly seen in the model results at 1600 EST, shown in Fig. 12. We see from Fig. 12 (top) that due to surface downdraft cooling, the original sea breeze convergence zone has become associated with downward motion, while on its east and west sides upward motion occurs. The simulated rainfall map at 1600 EST (Fig. 12, bottom) shows that the peak rainfall is located just to the north of Lake Okeechobee, being associated with the original west coast convection. Two new rainfall peaks can be seen along the west coast: one to the southwest of the lake, and the other around Tampa. It is also seen (comparing Fig. 13 with Fig. 6) that the southern part of the peninsula became essentially free of convection by this time. The original tendency for elongated convective zones have become replaced by locally enhanced convective systems by 1600 EST. This indicates that the mature convective development is no longer completely within the original sea breeze convergence zones which formed a few hours earlier.

Finally, model results at 1700 EST are shown in Fig. 14. We see that the basic pattern from the previous hour is retained except that the new convective development along the west coast has become rather significant. In the area between this new west coast convection and the older convection (which is to the immediate north and south of the lake) we see a region of downward motion (Fig. 14, top). The surface radar rainfall at 1700 EST (Fig. 15) shows clearly that the convection existing an hour ago (Fig. 13) has diminished, and that there are new convective developments surrounding the earlier convective area. The newly

7

developed coastal convective systems can be seen to have been simulated in the model (Fig. 14, top).

In summary, we see that the summertime Florida convective-environmental interactions along the west coast have been simulated by the numerical approach utilized in this study to the extent that the model has produced the locations of favored deep convective patterns over the Florida peninsula during the synoptically undisturbed days.

It is seen that the model has successfully produced features which have been revealed by previous investigations. These include: (a) a merging process (Simpson *et al.*, 1980) associated with both downdraft cooling and the sea breeze forcing; (b) localized reduction of the sea breeze convergence due to the downdraft cooling effect (Burpee, 1979; Cooper *et al.*, 1982; and Burpee and Lahiff, 1984); and (c) an inland propagation of the coastal convective system produced by the combination of a sea breeze propagation (Frank *et al.*, 1967) and a propagation associated with the downdraft cooling effect in the lower troposphere.

4   Discussion

4.1   Mesoscale Tropospheric Circulation

Convective-produced effects on the surface sea breeze flow have been illustrated in the previous section. This subsection discusses the deep convective effects upon the upper troposphere.

Unfortunately, however, very little has been reported in the literature concerning deep convective-induced mesoscale tropospheric circulations for the peninsular-scale Florida environment. Therefore, it is necessary to compare several of the model results with observed deep convective activities in other areas.

In this section, XZ-cross sections (at the latitude indicated by the line AB in Fig. 11) will be shown for the pure-convectively induced (i.e., "total-dry") tropospheric mesoscale

8

circulations. The vertical circulations will be illustrated only for 1500 EST and 1600 EST, sine deep convective effects were most developed during this period.

First we see from Fig. 16 (top) that at 1500 EST, the deep convection produced a "cooling-warming-cooling" pattern with height on the resolvable-scale potential temperature field. This pattern is caused by, respectively, cloud top overshoot cooling (including the cooling of adiabatic expansion associated with the mesoscale upper tropospheric ascent, Fritsch and Brown, 1981); net convective heating; and surface downdraft cooling. The result of this heating profile is a "divergence-convergence-divergence" pattern in the horizontal flow (Fig. 16, bottom).

Due to the heating pattern described above, a "four-cell" vertical solenoidal circulation pattern is evident in the horizontal u-velocity field (Fig. 17, top) and the y-direction vorticity field (Fig. 17, bottom) (i.e., due to upper divergence; mid-level convergence and surface divergence). The production of such a four-cell circulation pattern indicates that the deep convective effect upon the mesoscale environment is not uniform in the vertical (i.e., not a single vertically stretched solenoidal circulation). Rather, deep cumulus convection appears to enhance mid-tropospheric horizontal convergence, while producing surface divergence due to downdraft cooling which then enhances surface convergence in the surrounding area. This statement is consistent with the fact that, in the absence of an upper-level synoptic-scale disturbance, Florida's upper troposphere (above about 5 km) is free of horizontal divergences when only the dry sea breeze (without cumulus convection) exists. Thus, the convective induced warming of the mid and upper tropospheric mesoscale environment and cooling in the lower troposphere is directly responsible for the generation and enhancement of mid-tropospheric convergence. Johnson and Kriete (1982) described a similar cloud-induced upscale development in their tropical deep convective analysis. The vertical motion field and the vertical component of vorticity at 1500 EST are shown in Fig. 18 (top) and 18 (bottom), respectively.

9

The mesoscale model used in the current study does not include latent heat release on the resolvable-scale field (i.e., all moist processes are produced in the convective parameterization). Therefore, this model may not be able to generate the mesoscale updraft/downdraft discussed in Zipser (1977), Leary and Houze (1979), and Houze (1982), among others. In spite of this, however, the above results are very similar to an observed composite mid-latitude squall line documented in Ogura and Liou (1980). Since Ogura and Liou (1980) considered quantities which are on a relative coordinate framework moving with the observed squall line, the dynamic and thermodynamic structures in their study are comparable to the corresponding "total-dry" quantities illustrated in the current study (the differences will be discussed below). Comparing Fig. 16 (bottom) with their figures (13, 15, 16 and 18), we see that in both cases, there is a slantwise convergence zone in the vertical cross section which extends from the front (relative to the surface flow) of the system at the surface to the upper troposphere, with divergence zones above and below the maximum convergence. The result of these convergences are two upward motion centers: one near 700 mb and an upper one near 400 mb, and a downward motion center near 700 to 800 mb. Related to these are the vorticity fields and the horizontal wind components which also closely correspond to the results shown in Fig. 17 (top). It can be seen, for example, that the low-level environmental inflow becomes elevated as it approaches the convective system.

The above described resemblance between the current study and Ogura and Liou (1980) must be interpreted realizing a difference existed in the background vertical wind profile between the two cases. The background large-scale wind considered in the current study has an easterly maximum in the upper troposphere with weaker easterly winds in the mid- and lower-troposphere. This wind structure is different from that in Ogura and Liou (1980) in which a westerly jet dominated the upper troposphere. In their study, it was stated that around the midtroposphere (during the lifetime from the mature stage to the decaying

stage), the westerly background momentum opposes the easterly momentum which is carried upward by the low-level inflow. The result of this is a mid-tropospheric convergence. The mid-level inflow from the rear of the system was indicated to be primarily responsible for generating a mesoscale downdraft through evaporational cooling by providing an input of relatively dry air (Zipser, 1977; Brown, 1979). In the current study, the midtropospheric convergence is convectively-driven and enhanced by the downdraft-cooling induced surface convergence surrounding the convection (which elevates the low-level inflow) and convective-heating induced upper tropospheric divergence. The comparison with the Ogura and Liou (1980) study is discussed further using the sensitivity experiments presented in section 4.2.

By 1600 EST, Fig. 19 (top) shows that the resolvable-scale warming/cooling pattern becomes somewhat more complicated. A newly formed cooling-warming "dipole" is found around the mid-to-lower troposphere in the original convective area (the system has moved eastward). The general structure of the kinematic quantities, however, are basically retained as seen in the horizontal divergence (Fig. 19, bottom) and the horizontal u-velocity (Fig. 20, top) fields. Comparing the vertical motion structure (Fig. 21, top) with the tempera-ture field (Fig. 19, top), we see that the newly formed mid-tropospheric cooling/warming dipole is associated with adiabatic cooling due to mesoscale upward motion and subsidence warming due to mesoscale downward motion, respectively.

4.2 Peninsula-Scale Convergence

In order to see the effects of the imposed large-scale wind profile upon the above described convective feedbacks, two extra simulations were performed which differ from the control run only in the initial wind profile and are otherwise exactly the same. In one simulation, the winds in the upper troposphere (above about 5 km) are the mirror images of those in the control run (i.e., with a westerly maximum replacing an easterly maximum in the upper troposphere), while preserving the same winds in the lower troposphere (thus this wind structure corresponds to that in Ogura and Liou, 1980, although with smaller peak values).

11

The second sensitivity simulation is initialized with zero large scale wind throughout the domain.

Results indicate that there are quantitative differences in the convective feedback quantities between the control and the two sensitivity simulations during the afternoon period. Qualitatively, however, the three simulations consistently indicate the generation of mid-tropospheric convergence and positive vorticity over the mesoscale domain during the mature and decaying stage of the convective system. Fig. 22 shows the horizontal (about 350 km x 350 km) averaged horizontal divergence and the vertical component of vorticity at the three times indicated and for the three simulations. From Fig. 22, we can see that during the afternoon period (1400 EST to 1600 EST), the peninsula-averaged surface convergence ceased growing, as also indicated by Burpee (1979) and Cooper *et al.* (1982). In the upper troposphere, however, there appear to be rather significant time-variability in the convectively-induced peninsula-scale vertical mass profile. Relatively significant peninsula-averaged upper tropospheric divergence (above 9 km), mid-tropospheric convergence (between 3 and 9 km) and lower tropospheric divergence (between 1 and 3 km) can be seen (Fig. 22, bottom left) to be coupled with the near surface convergence (within the lowest 1 km). Accordingly, positive vorticity is generated in the mid-tropospheric layer between about 4 and 10 km, particularly for the upper-westerly simulation (the vorticity values for the upper-easterly and the no-wind simulations are somewhat smaller).

Burpee and Lahiff, (1984) indicated that, for a sea breeze day in south Florida with a relatively unstable lower troposphere, the morning surface divergence and a nearly non-divergent middle troposphere (at 0700 EST) changed to a dramatically different profile (i.e., convergence below 900 mb, divergence between 900 and 700 mb, convergence between 700 and 300 mb and divergence between 300 and 150 mb, at 1900 EST). It is informative to compare the model results of the peninsula-averaged divergences (Fig. 22) with the observed divergences documented in their analysis. We note that the input sounding used

12

for the model runs (Fig. 1 of Part I) has a temperature difference between 950 mb and 600 mb of about 22°C and a rather high layer averaged relative humidity (RH> 60%). Therefore, the model situation does not fall exactly into the "least stable" category (but, however, is closer to this category than others) of Burpee and Lahiff (1984). Furthermore, the computational domain (see their Fig. 1) for their surface divergence is not the same as that for the upper divergence, and does not include the southwest portion of south Florida (which, as we have seen, is often associated with significant sea breeze-induced surface convergences). Despite these and other differences, however, we found several consistent and therefore encouraging results between the observed and simulated (Fig. 22) peninsula-scale divergences. For example, the observed and modeled near surface convergences in the late afternoon are both in the range of -2.0 to -16.0 x 10^{-6} s^{-1}. The lower tropospheric divergence for the least-stable category in the Burpee and Lahiff study (between 1 and 3 km, peak values of around $+4.0$ x 10^{-6} s^{-1}) agrees well with the model (between 1 and 3 km, peak values of around $+4.0$ x 10^{-6} s^{-1}). The mid-tropospheric convergence observed for the least-stable case (between 3 and 9 km, peak values of around -2.0 x 10^{-6} s^{-1}) agrees well with the model (between 3 and 9 km, peak values of around -4.0 x 10^{-6}). Thus, the model simulation results agree well with observations of the peninsula-scale divergence profile during the late afternoon on a sea breeze day with a generally convectively-favorable initial large-scale environment.

As discussed in Burpee and Lahiff (1984), the peninsula-scale divergence profiles are similar to that presented by Gamache and Houze (1982), and Johnson and Kriete (1982). The physical mechanism regarding the effects of the mesoscale descent motion (once generated) to subsequent deep convective storm evolution, however, was not discussed in Burpee and Lahiff (1984), or Johnson and Kriete (1982). The storm evolution during the late mature stage is discussed in the next subsection.

4.3 Mid-Tropospheric Asymmetry

The physical significance of the mid-tropospheric convergence generated during the mature stage of a mesoscale convective system is related to a mechanism which either enhances the system or drives the system from mature to the dissipating stage. Fig. 23 shows the resolvable-scale moisture flux in the XZ-cross section (as used in Figs. 16 to 18) for 1500 EST (top) and 1600 EST (bottom). Positive-valued regions are areas with upward transport of the low-level high humidity air, while negative-value regions indicate the downward transport of higher-level low-humidity air. It is seen from Fig. 23 (top) that the mid-tropospheric convergence at 1500 EST (Fig. 16, bottom) is associated with a highly asymmetric thermodynamics field surrounding the convective system. That is, relatively moist air is advected from the low-level front-side of the system upward toward the center of the system. Meanwhile, drier air is entering the convective system from the rear side in the mid-troposphere which then descends. Therefore, a mature stage occurs when there exist a near-balance between the moist front-to-rear jet (MFJ) originating in the moist planetary boundary layer and a dry rear-to-front jet (DRJ) originating in the mid-troposphere (the MFJ and the DRJ are indicated in Fig. 23 and the associated horizontal and vertical flows indicated in Figs. 17 (top) and 18 (top). A break-up of such a near-balanced state would then indicate either a further enhanced convective development (i.e., if the MFJ dominates) or a dissipating stage (i.e., if the DRJ dominates). The latter can be seen from the 1600 EST structure in Fig. 23 (bottom), in which the center of the system has moved inland. As evident in Fig. 23 (bottom) the late mature stage of the system at 1600 EST is associated with a gradually reduced moisture supply due to the lower tropospheric downward motion which is enhanced by the evaporational cooling. That is, the downward motion gradually covers a large horizontal area underneath the major convective heating region, thereby further reducing the moisture supply from the surface. A continuation of such a situation leads to the dissipation of this convective system.

14

4.4 Conceptual Model

The evolution of deep cumulus convection in Florida's sea breeze environment has been discussed in the present study. It was found that two important processes are necessary conditions for Florida's summertime deep convection to develop: i) the ascent and continuous moisture enrichment of the boundary layer by the sea breeze; and ii) the moisture enrichment associated with the convectively-induced tropospheric mesoscale circulation. Since these two processes typically have time differences between them, it is important to see how the deep convective activities interact with the sea breeze circulation at different stages of the convective lifetime.

To obtain qualitatively representative circulation structures for each stage, the control run results are averaged in time over each of the following 2 hour periods:

- sea breeze convergence stage (stage 1): 1200-1400 EST

- convective downdraft cooling stage (stage 2): 1400-1600 EST

- decaying stage (stage 3): 1600-1800 EST.

Fig. 24 shows the conceptual model for the sea breeze-convective interaction at stage 1 for the chosen synoptic physical background. We see that the interrelationship at this stage is such that the embedded convection is supported by the direct heat and moisture supply provided by the sea breeze convergence. Along the west coast, the vertical motion associated with the original sea breeze circulation is enhanced and extended over a much thicker layer throughout the troposphere due to the deep convective effect.

Fig. 25 shows that in the sea breeze convergence stage, the maximum surface convergence region (along the west coast, as shown in Fig. 25a) coincides with the maximum surface .vorticity region (Fig. 25b). As discussed in Orlanski and Ross (1984), this indicates that the feedback effect produced by the embedded deep convection is to enhance the mesoscale upward motion generated by the original sea breeze convergence.

15

Fig. 26 shows the conceptual model for the sea breeze-convective interaction at stage 2. We see from Fig. 26 that there is a generation of a cool layer of air by deep convective downdrafts in the area of the original convection in stage 1. This results in both new deep convective growth on the low-level, upwind side of the convective system, and the stabilization underneath the old convection. The combined effect permits the convective system to propagate in the upwind direction where the moisture supply is richer. The result of both the low-level downdraft cooling effect and the enhanced mid-tropospheric convergence is to produce a four-cell solenoidal circulation pattern, as distinguished from a two-cell solenoidal circulation in stage 1 (Fig. 24).

Fig. 27 shows that during the convective downdraft cooling stage, the maximum surface convergence region is not as regular as it is in stage 1. Rather, the locations of the surface convergence maxima are determined by the combined forcing of the surface sea breeze flow and the downdraft cooling effect (as discussed previously). As seen in Fig. 27a, the surface convergence maximum located just to the west of the lake has propagated inland, which is therefore separated from the corresponding surface vorticity maximum (Fig. 27b). As discussed in Orlanski and Ross (1984), such a phase shift between the surface convergence maximum and surface vorticity maximum indicate that the convergence no longer acts to strengthen the original convective zone (or frontal zone in their case).

As discussed previously, during the mature stage of the convective lifetime the downdraft cooling effect is seen to provide a positive feedback mechanism which enhances the subsequent convection by generating low-level front-side upward motion; meanwhile the downdraft tends to stabilize the original convective area by replacing the original boundary layer air with colder air. The mid-tropospheric convergence is related to the mesoscale upward and downward motion during the late afternoon. The downward motion acts to decrease the low-level moisture supply. Meanwhile, the surface convergence produced by the downdraft cooling effect tends to propagate away from the convective system, thereby

decreasing the connection between the low-level moisture supply and the main convective system. The result of these processes, in addition to the reduction in sea breeze intensity as the sun sets, is that the system enters into its decaying stage. Fig. 28 shows that during the decaying stage mesoscale motions occur in response to the combination of the convectively-induced upper-tropospheric warming, mid-tropospheric convergence and the lower-tropospheric downdraft cooling effect. Weaker surface convergences are still generated surrounding the old convective system. However, since the sea breeze flow is controlled by the diurnal solar cycle and surface solar heating has diminished, further deep cumulus convective development is not expected during stage 3.

5 Conclusion

The space-time mesoscale-convective interactions in Florida's sea breeze environment over both the time period of deep convection and over the peninsula-scale domain have not been extensively documented in the literature. The current study provides such a study. A mesoscale, hydrostatic primitive-equation model, originally developed by Pielke (1974) and Pielke and Mahrer (1978) is coupled with a newly derived convective parameterization which is formulated based on the discussions in Fritsch and Chappell (1980), Song and Frank (1983) and Frank and Cohen (1985). The model is applied to a synoptically undisturbed day over south Florida, with a large scale southeasterly wind. Model results are compared with available observations from several studies.

Summarizing the numerical simulations, it is found that the model is able to reproduce observed favored deep cumulus convective patterning over the Florida peninsula during synoptically undisturbed days. In particular, it has been shown that the model has successfully produced features which have been revealed by observations and previous investigations. These include: (a) a merging process associated with both convective-scale downdraft cooling and mesoscale sea breeze forcing (Simpson et al., 1980); (b) localized reduction of the sea

17

breeze convergence due to the downdraft cooling effect (Burpee, 1979; Cooper *et al.*, 1982; Burpee and Lahiff, 1984); and (c) an inland propagation of the coastal convective system produced by the combination of a sea breeze propagation (Frank *et al.*, 1967; Pielke, 1974) and a propagation associated with the downdraft cooling effect at the surface (Byers and Braham, 1949).

The preconditioning and continuous enrichment of the convective area provided by the mesoscale sea breeze circulation appears to be a necessary condition for Florida's deep convection to develop on synoptically undisturbed days. The convective-environmental interrelationship during the earlier stage of the convective lifetime is such that the embedded convection is located coincident with the sea breeze convergence zones, and is supported by the moisture and heat enrichment of the sea breeze. Following the onset of significant cooling in the lower troposphere associated with convective downdrafts, the region of deep convection propagates away from the original sea breeze convergence areas.

One important convective feedback effect upon the mesoscale environment is a surface convergence (generated by the downdraft cooling and resultant mesoscale circulation and inflows due to the sea breeze convergence) which elevates the low-level environmental flow when the latter approaches the convective system. Since this inflow air stream advects moisture from the boundary layer to the mid-troposphere, it serves as an important fuel supply to subsequent convective development (this air stream is denoted as a moist front-to-rear jet, or MFJ). On the rear side of the system, there is inflow enhanced by a mid-tropospheric horizontal convergence and a lower-tropospheric convectively-induced evaporational cooling (this inflow air stream is denoted as a dry rear-to-front jet, or DRJ). During the mature stage of the system, deep convective effects are such that they produce a "four-cell" tropospheric circulation pattern. If the mature stage becomes steady state, there would be a balance between the MFJ and the DRJ. The loss of such a near-balanced state would indicate either further enhanced convective development (i.e., if the MFJ dominates) or

a decaying stage (i.e., if the DRJ dominates). A comparison between the model results and the observational analysis of Burpee and Lahiff (1984) indicates that the model has produced results which are at least qualitatively consistent with observations.

As a suggested further study, the convective parameterization derived in this study will be examined thoroughly, using a high-resolution explicit simulation approach on the same space and time domains, in order to determine its feasibility and accuracy of representing deep convective effects on the mesoscale. The Florida environment will be initially chosen as the physical background for such a "implicit vs. explicit" investigation (Molinari and Dudek, 1986). However, further investigations will be performed which incorporate orographic and/or frontal environmental forcing which are not included in the Florida studies.

6 Acknowledgements

7 References

Brown, J. M., 1979: Mesoscale unsaturated downdrafts driven by rainfall evaporation: A numerical study. *J. Atmos. Sci.*, **36**, 313-338.

Burpee, R. W., 1979: Peninsula-scale convergence in the south Florida sea breeze. *Mon. Wea. Rev.*, **107**, 852-860.

Burpee, R. W. and L. N. Lahiff, 1984: Area averaged rainfall variations on sea-breeze days in south Florida. *Mon. Wea. Rev.*, **112**, 520-534.

Byers, H. R. and R. R. Braham, Jr., 1949: The Thunderstorm. U.S. Government Printing Office, Washington, D.C., 287 pp. [NTIS PB-234515].

Cooper, H. J., M. Garstang and J. Simpson, 1982: The diurnal interaction between convection and peninsular-scale forcing over south Florida. *Mon. Wea. Rev.*, **110**, 486-503.

Frank, N. L., P. L. Moore and G. E. Fisher, 1967: Summer shower distribution over the Florida peninsula as deduced from digitized radar data. *J. Appl. Meteor.*, **6**, 309-319.

Frank, W. M. and C. Cohen, 1985: Properties of tropical cloud ensembles estimated using a cloud model and an observed updraft population. *J. Atmos. Sci.*, **42**, 1911-1928.

Fritsch, J. M. and C. F. Chappell, 1980: Numerical prediction of convectively driven mesoscale pressure systems. Part I. Convective parameterization. *J. Atmos. Sci.*, **37**, 1722-1733.

Fritsch, J. M. and J. M. Brown, 1982: On the generation of convectively driven mesohighs aloft. *Mon. Wea. Rev.*, **110**, 1554-1563.

Gamache, J. F. and R. A. Houze, Jr., 1982: Mesoscale air motions associated with a tropical squall line. *Mon. Wea. Rev.*, **110**, 118-135.

Houze, R. A., Jr., 1982: Cloud clusters and large scale vertical motions in the tropics. *J. Meteor. Soc. Japan*, **60**, 396-409.

Hsu, S., 1969: Mesoscale structure of the Texas coast sea breeze. Report No. 16, Atmospheric Science Group, College of Engineering, University of Texas, Austin.

Johnson, R. H. and D. C. Kriete, 1982: Thermodynamic and circulation characteristics of winter monsoon typical mesoscale convection. *Mon. Wea. Rev.*, **110**, 1898-1911.

Leary, C. A. and R. A. Houze, Jr., 1979: The structure and evolution of convection in a tropical cloud cluster. *J. Atmos. Sci.*, **36**, 437-457.

McQueen, J. T. and R. A. Pielke, 1985: A numerical and climatological investigation of deep convective cloud patterns in south Florida. Atmos. Sci. Paper #389, Department of Atmospheric Science, Colorado State University, Fort Collins, Colorado, 177 pp.

Michaels, P. J., R. A. Pielke, J. T. McQueen and D. E. Sappington, 1987: Composite climatology of Florida summer thunderstorms. *Mon. Wea. Rev.*, **115**, 2781-2791.

Molinari, J. and M. Dudek, 1986: Implicit versus explicit convective heating in numerical weather prediction models. *Mon. Wea. Rev.*, **114**, 1822-1831.

Ogura, Y. and M. T. Liou, 1980: The structure of a mid-latitude squall line: A case study. *J. Atmos. Sci.*, **37**, 553-567.

Orlanski, I. and B. B. Ross, 1984: The evolution of an observed cold front. Part II: Mesoscale dynamics. *J. Atmos. Sci.*, **41**, 1669-1703.

Pielke, R. A., 1974: A three-dimensional numerical model of the sea breeze over south Florida. *Mon. Wea. Rev.*, **102**, 115-139.

Pielke, R. A., 1984: *Mesoscale Meteorological Modeling.* Academic Press, New York, NY, 612 pp.

Pielke, R. A. and W. R. Cotton, 1977: A mesoscale analysis over south Florida for a high rainfall event. *Mon. Wea. Rev.*, **105**, 343-362.

Pielke, R. A. and Y. Mahrer, 1978: Verification analysis of the University of Virginia three-dimensional mesoscale model prediction over south Florida for 1 July 1973. *Mon. Wea. Rev.*, **106**, 1568-1569.

Reap, R. M. and D. S. Foster, 1979: Automated 12-36 hour probability forecasts of thunderstorms and severe local storms. *J. Appl. Meteor.*, **18**, 1304-1315.

Simpson, J., N. E. Westcott, R. J. Clerman and R. A. Pielke, 1980: On cumulus mergers. *Arch. Meteorol. Geophys. Bioklimatol. Ser.*, **A.29**, 1-40.

Song, J. L. and W. M. Frank, 1983: Relationships between deep convection and large-scale processes during GATE. *Mon. Wea. Rev.*, **111**, 2145-2160.

Song, J. L. and R. A. Pielke, 1988: The influence of deep cumulus convection on sea breeze dynamics over south Florida. Part I: Model development. Atmos. Sci. Paper #426, Department of Atmospheric Science, Colorado State University, Fort Collins, Colorado.

Zipser, E. J., 1977: Mesoscale and convective scale downdrafts as distinct components of squall line structure. *Mon. Wea. Rev.*, **105**, 1568-1589.
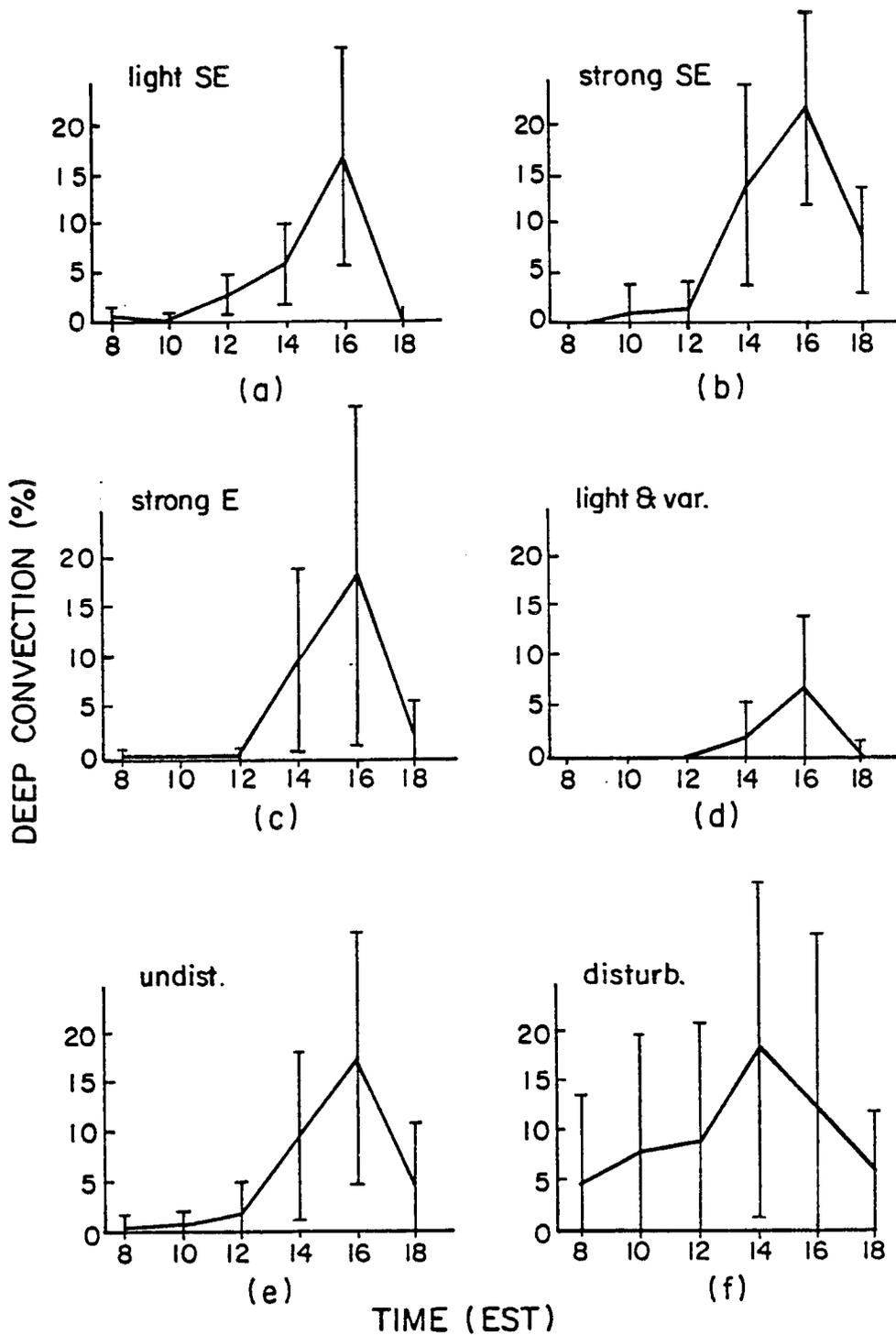
Figure 1 - Time series of the averaged percent of deep convective clouds for the various synoptic classes: a) light southeast, b) strong southeast, c) strong east, d) light and variable, e) undisturbed, and f) disturbed. The error bars corresponding to one standard deviation around the mean are also given (reproduced from McQueen and Pielke, 1985).
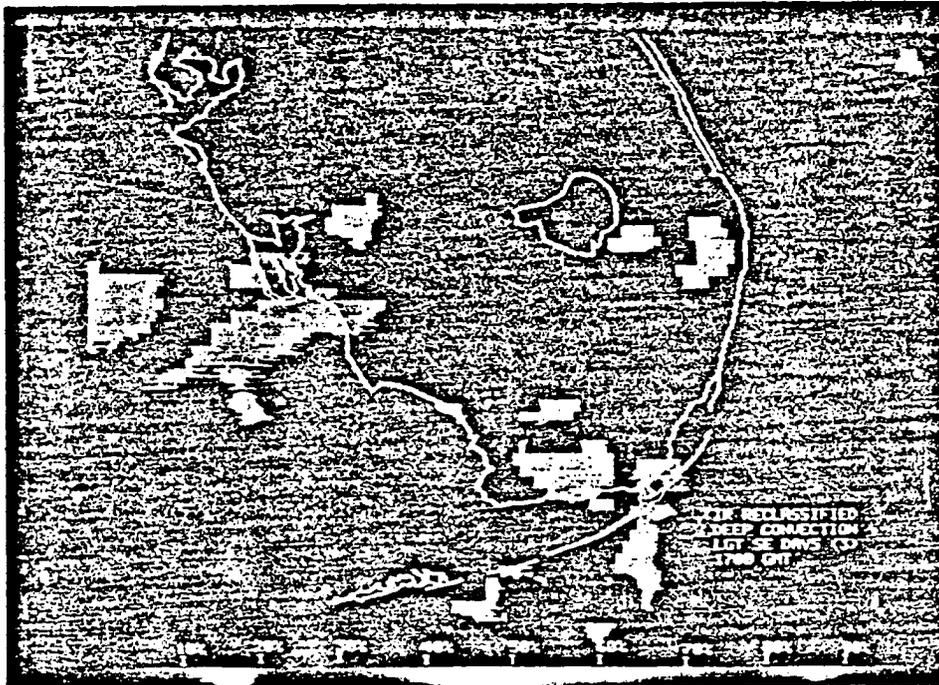
(a)
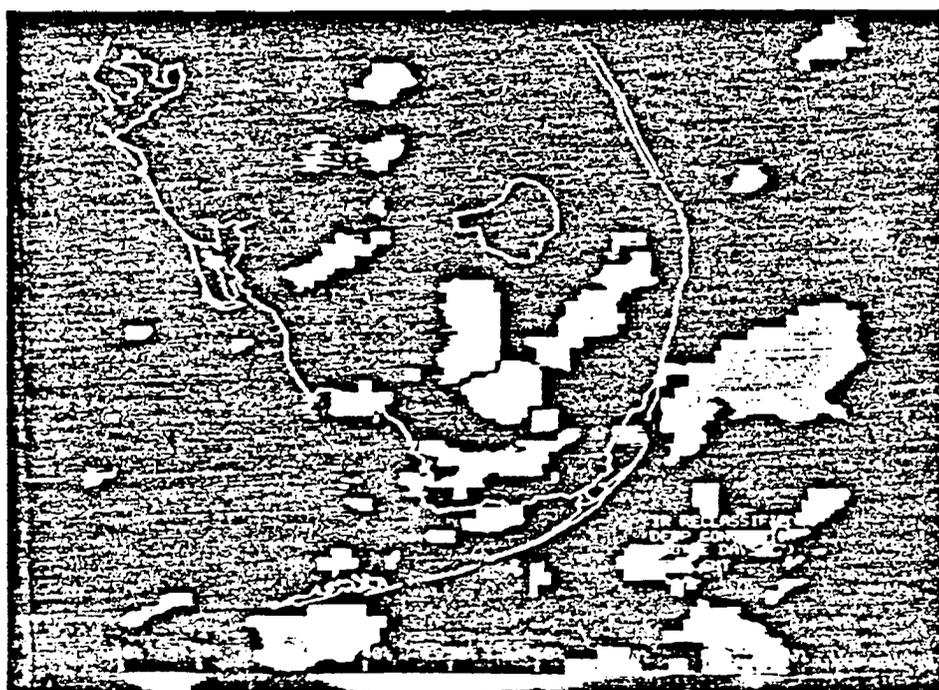
(b)

Figure 2a - Satellite image composites by synoptic flow for a) light southeast, b) strong southeast classes at 1200 EST. Bar on the bottom of image relates shading to cloud frequency (on originals, a color bar is used). The number in parentheses on each image label indicates the number of images which went into creating the composite. (Color slides of all the composites are available, which more clearly illustrate the cloud composite frequencies; costs prevented reproducing these figures in color in this paper (from McQueen and Pielke, 1985).

25

(a)

(b)

Figure 2b - Same as Fig. 2a except for 1400 EST.
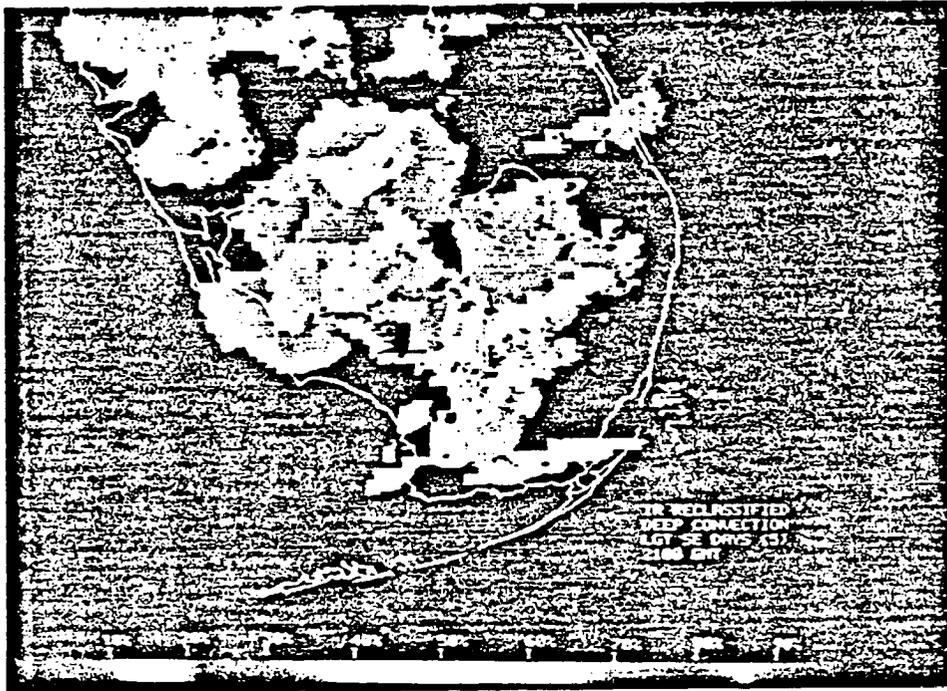
(a)

(b)

Figure 2c - Same as Fig. 2a except for 1600 EST.
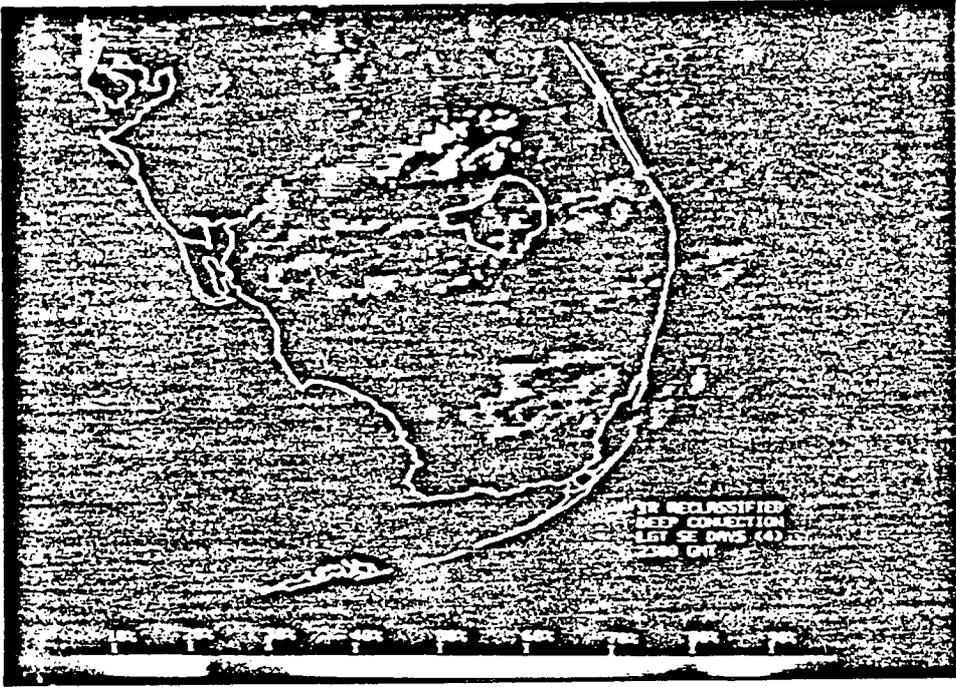
(a)
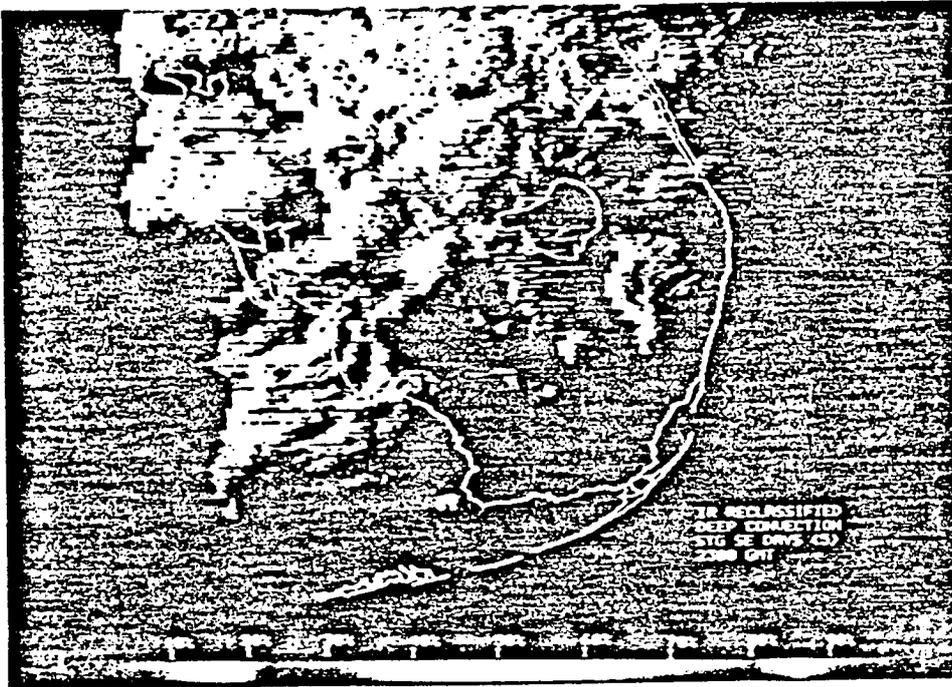
(b)

Figure 2d - Same as Fig. 2a except for 1800 EST.
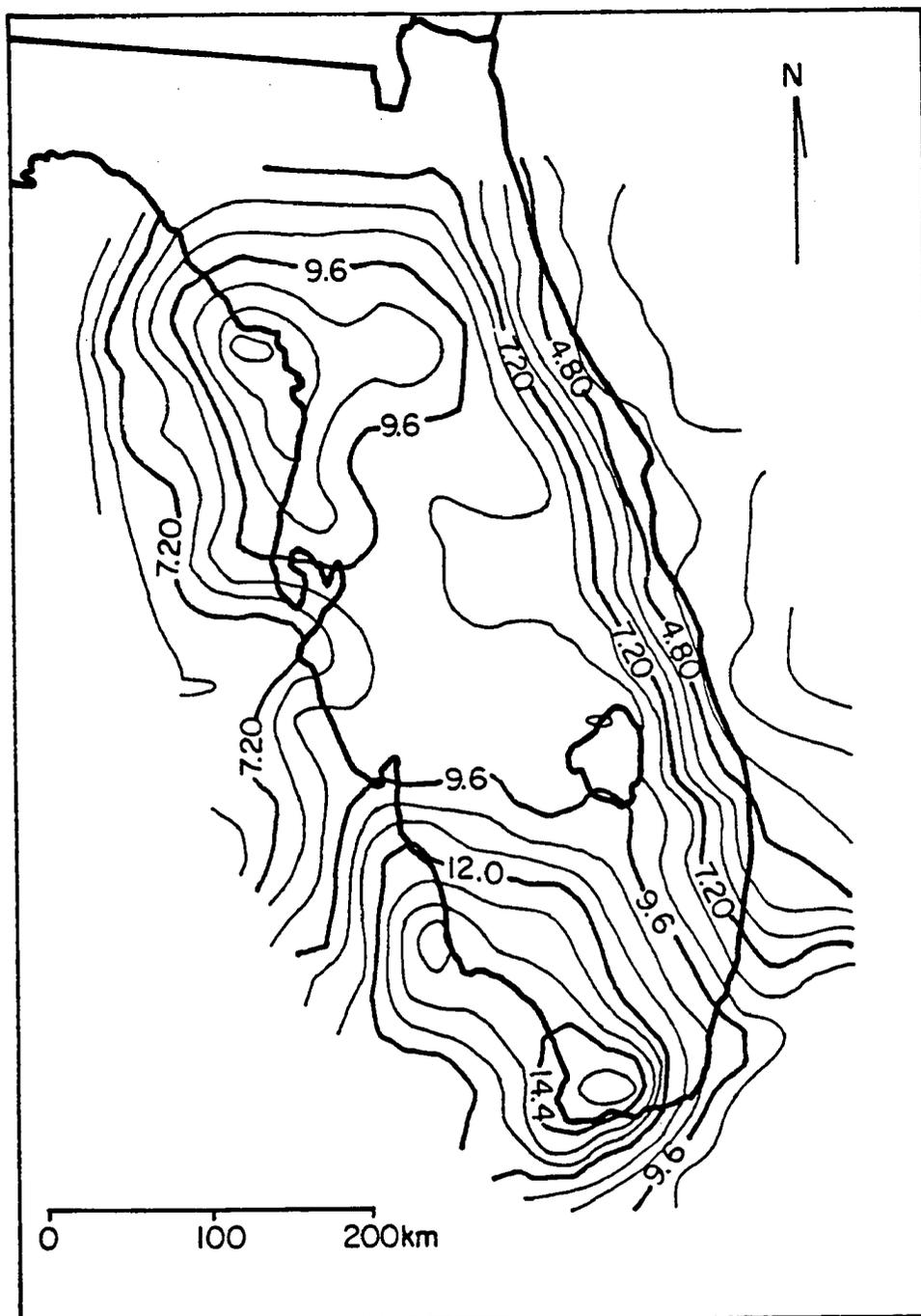
Figure 3 - Mean percent of hours that a MDR VIP return of 3.0 or greater was observed (from Michaels *et al.*, 1987).
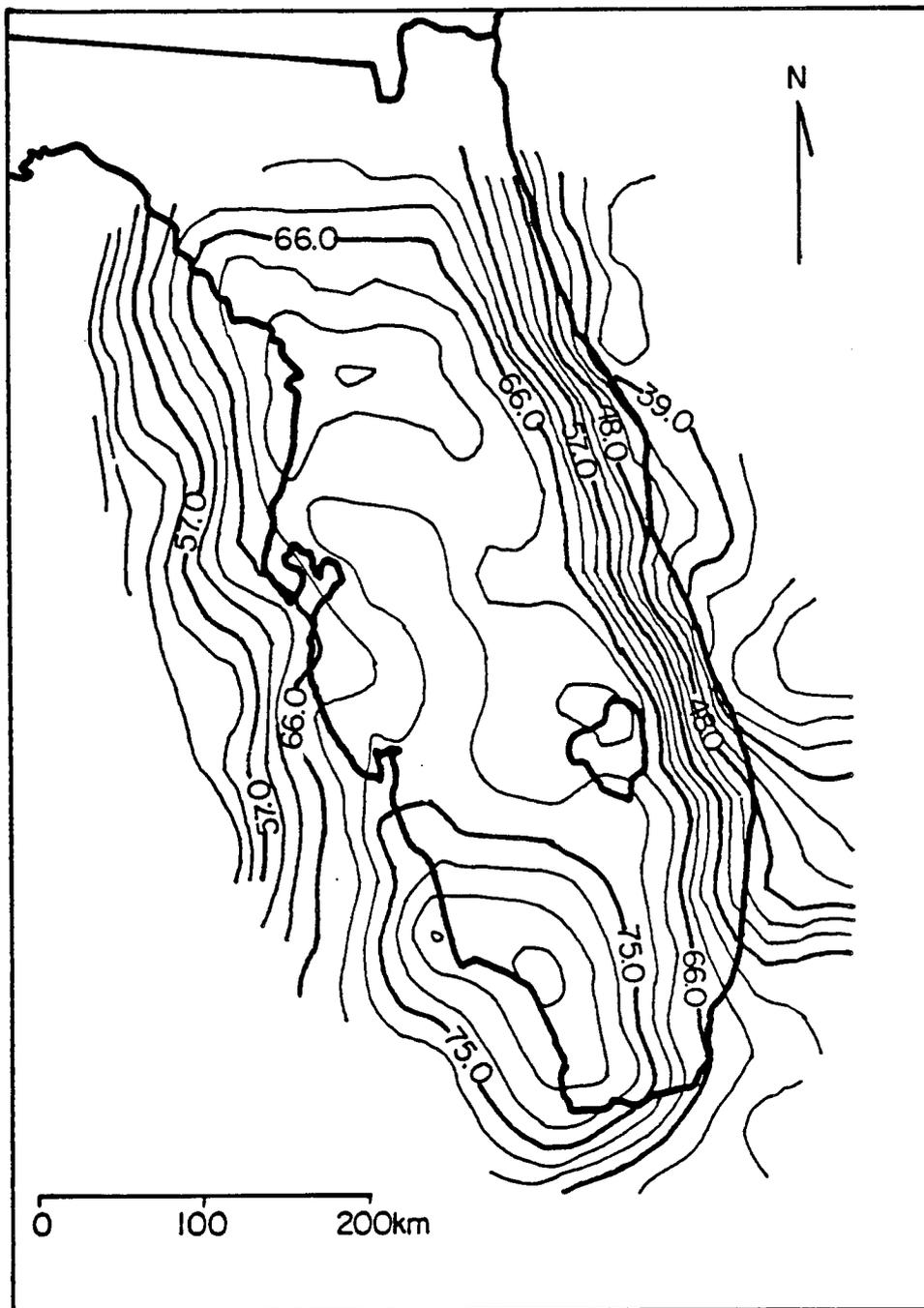
Figure 4 - Mean percent of summer (June-August) days in which a MDR VIP return of 3.0 or greater is observed (from Michaels *et al.*, 1987).
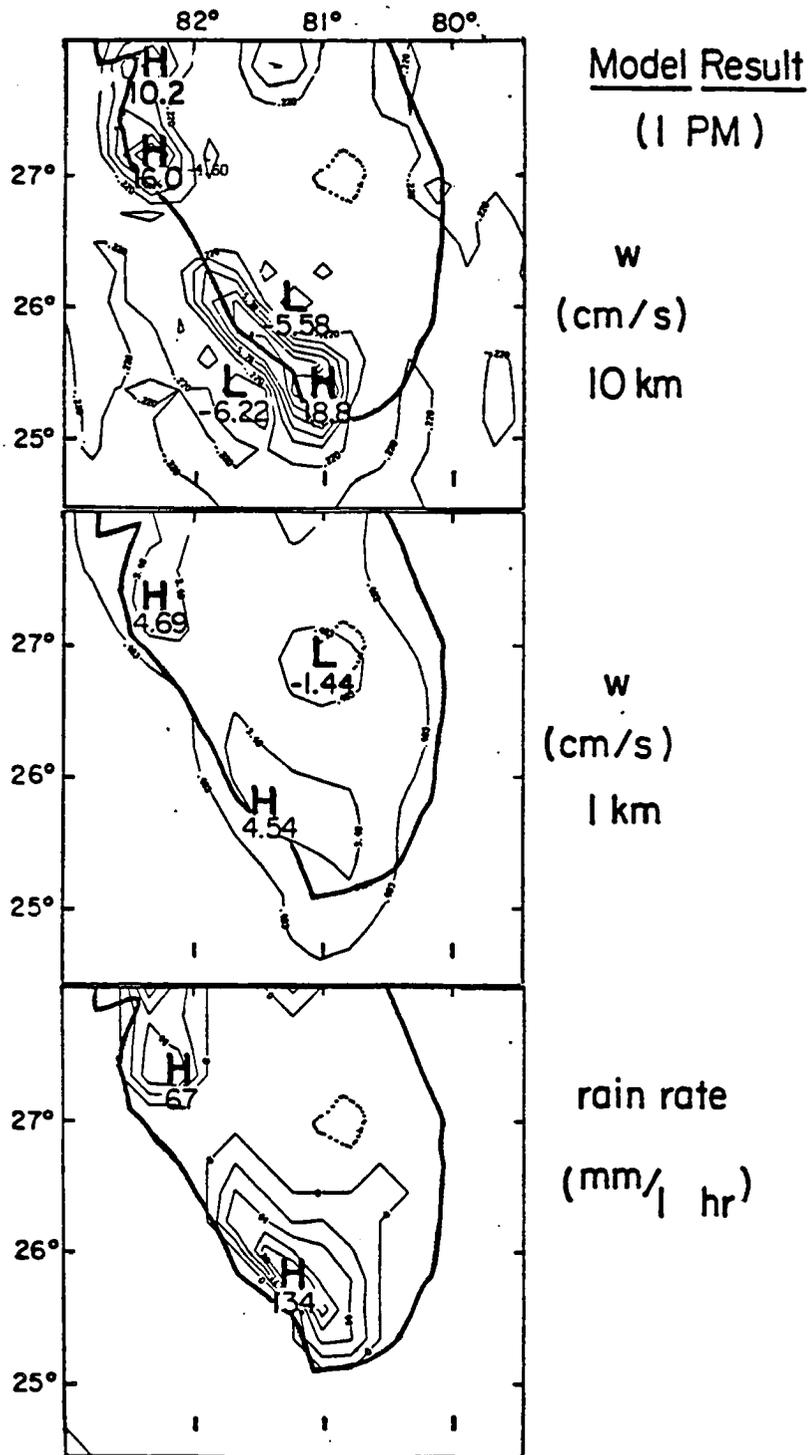
Figure 5 - The model produced horizontal maps of vertical velocity (cm/s) near 10 km (top) and 1 km (middle); and the model rainfall rate (mm/1 hour) (bottom), at 1 p.m. (1300 EST). The symbol "H" indicates upward motions, while "L" indicates downward motions. The contour interval for the velocities is 3 cm/s, and for the rainfall rates 2.2 mm/hour).
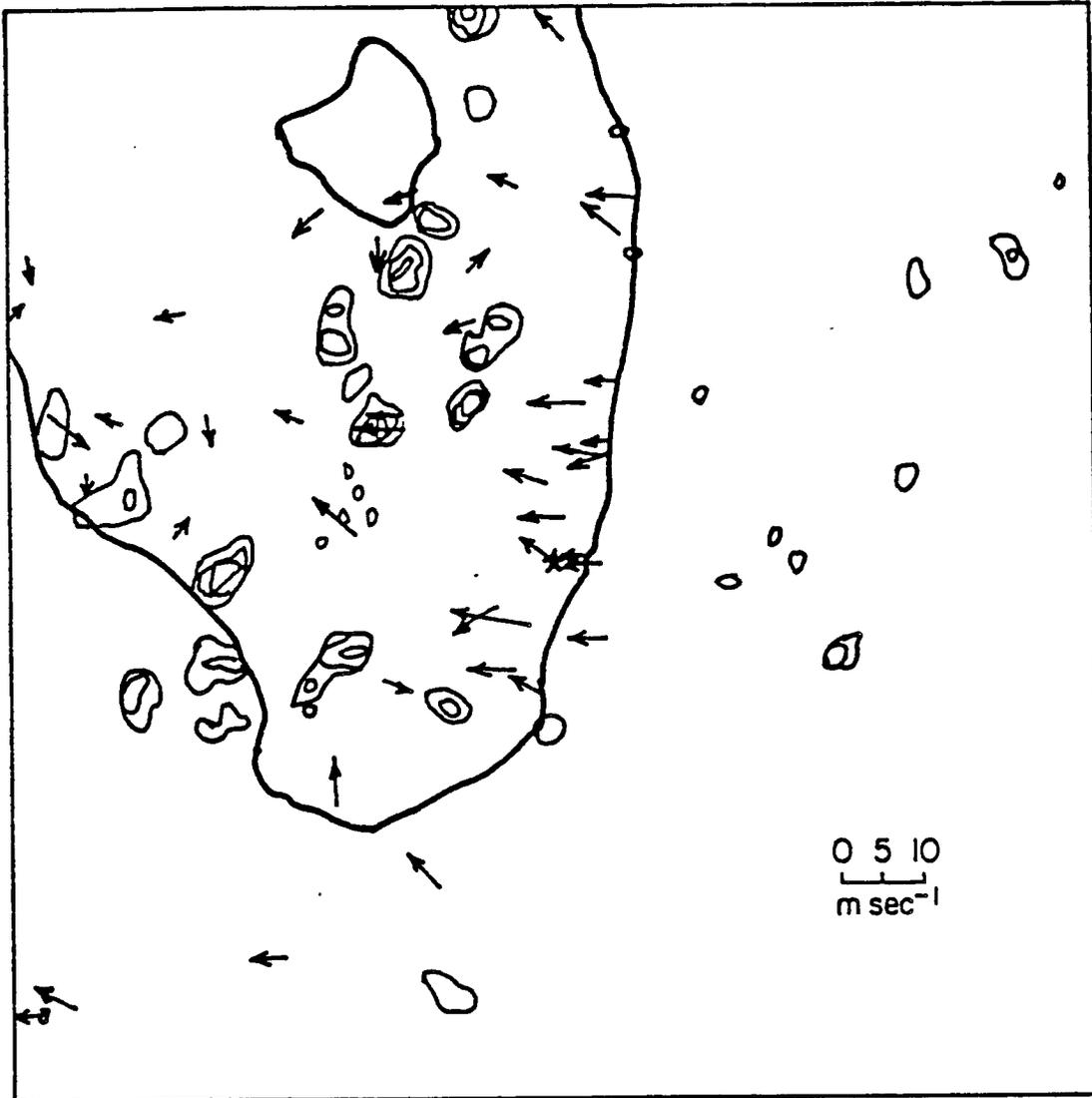
Figure 6 - Surface radar rainfall map at 1300 EST over southern Florida on 17 July 1973. The first contour indicates a rainfall rate of 0.25 mm/hr, while the second, third, and fourth indicate, respectively, rates of 2.29, 13.72, 30.23 mm/hr. Also included are the surface wind vectors.

Model Result

(2 PM)

w

(cm/s)

10 km

w

(cm/s)

1 km

rain rate

(mm/1 hr)
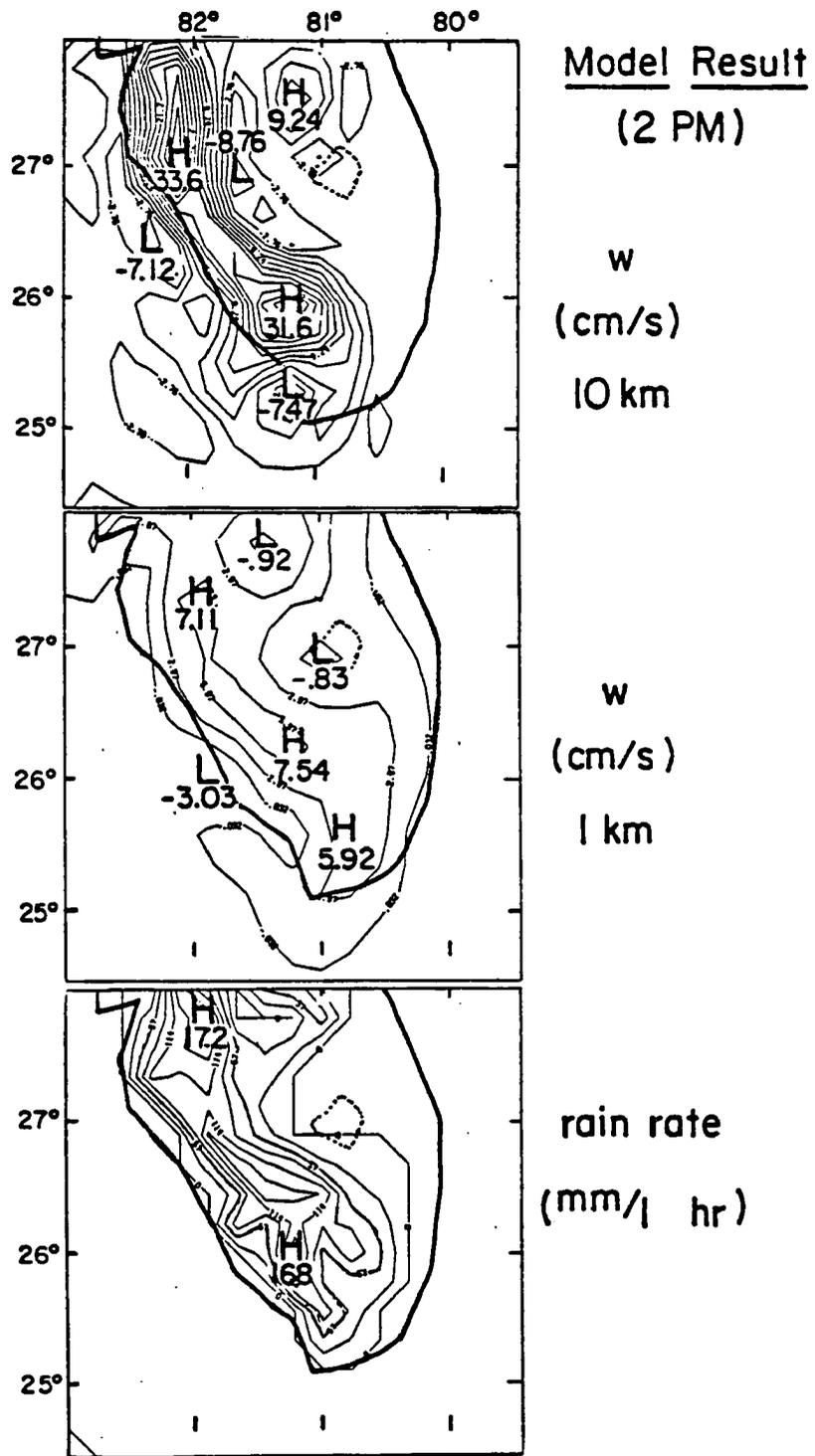
Figure 7 - Same as Fig. 5 but for 2 p.m. (1400 EST).
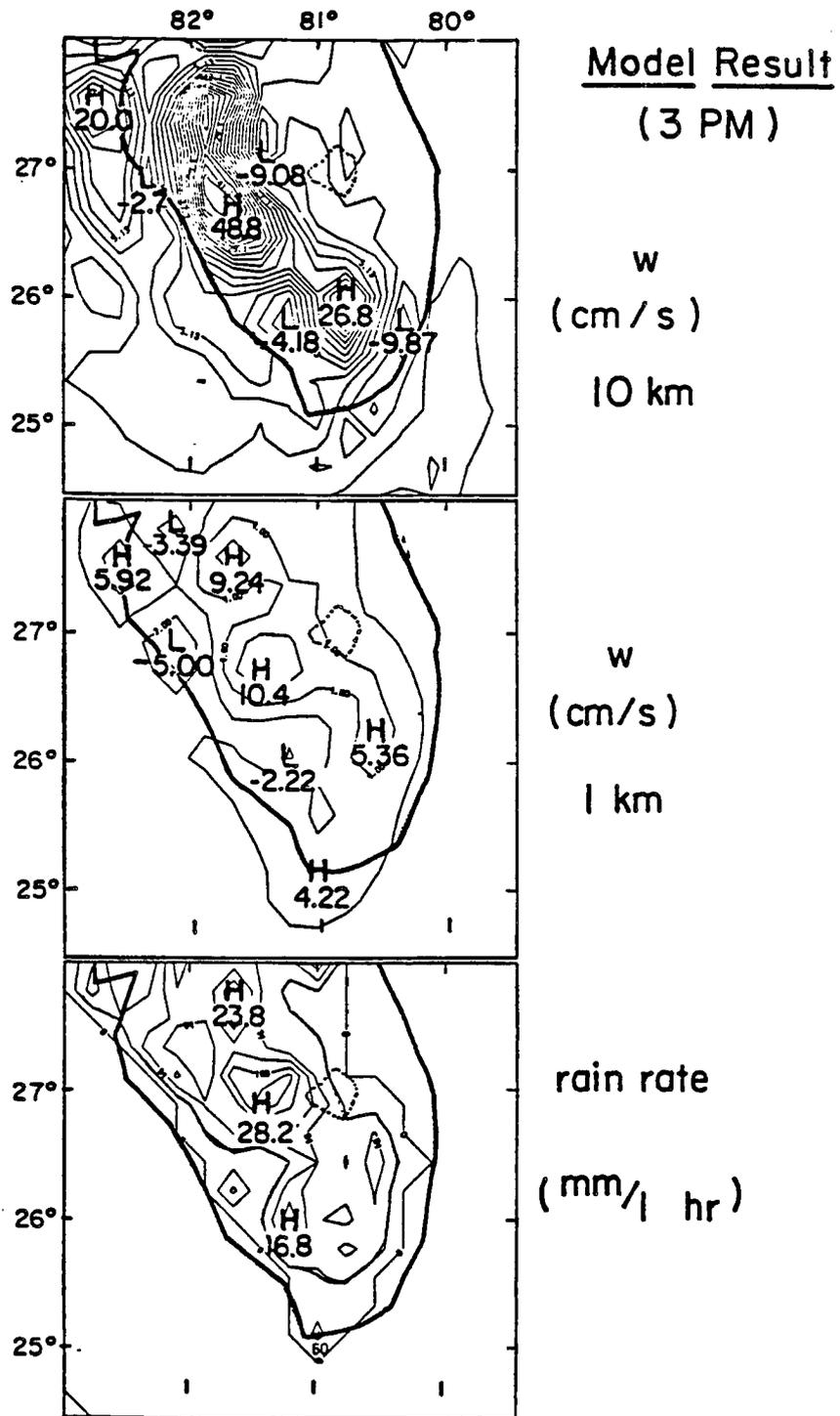
Figure 8 - Same as Fig. 5 but for 3 p.m. (1500 EST).

Figure 9 - Horizontal distributions at 9 m of model produced horizontal divergences at 1 p.m. (1300 EST). (10^{-4} s^{-1}) from the control run (indicated as "total") (top); and from the difference by subtracting a dry run result from the control run result (indicated as "total-dry" (bottom). "H" indicates divergence center and "L" indicates convergence center.

Figure 10 - Same as Fig. 9 but for 2 p.m. (1400 EST).

"total"

"total-dry"

Figure 11 - Same as Fig. 9 but for 3 p.m. (1500 EST).

Figure 12 - Same as Fig. 5 but for 4 p.m. (1600 EST).

Figure 13 - Same as Fig. 6 but for 4 p.m. (1600 EST).

Figure 14 - Same as Fig. 5 but for 5 p.m. (1700 EST).

Figure 15 - Same as Fig. 6 but for 5 p.m. (1700 EST).

Figure 16 - The "total-dry" potential temperature (K°, top) and horizontal divergence (10^{-4} s^{-1}, bottom) at 1500 EST, on the XZ-cross section indicated by the AB line in Fig. 11. The two coasts are indicated by the short vertical lines with "W" and "E" marks, respectively, shown on the bottoms of the XZ-cross section.

Figure 17 - Same as Fig. 16 but for horizontal u-velocity (m/s, top) and Y-direction vorticity $(10^{-4}\ s^{-1}$, bottom). For the letter, positive values correspond to clockwise rotation on the XZ-plane.

Figure 18 - Same as Fig. 16 but for vertical velocity (cm/s, top) and vertical vorticity (10^{-4} s^{-1}, bottom).

Figure 19 - Same as Fig. 16 but for 4 p.m. (1600 EST).

Figure 20 - Same as Fig. 17 but for 4 p.m. (1600 EST).

Figure 21 - Same as Fig. 18 but for 4 p.m. (1600 EST).

47

Figure 22 - Profiles of model horizontal divergence (left) and vertical vorticity (right) averaged over an area about 350 km x 350 km, at the three times indicated and for the three sensitivity simulations discussed in Section 4.2.

Figure 23 - Vertical grid-scale moisture fluxes (wq) at 1500 EST (top) and 1600 EST (bottom) on the XZ-cross section shown by the AB line in Fig. 11. The vertical velocity (w) is in cm/s, while model's specific humidity (q) is in kg/kg. The magnitudes shown in the figures are for the products wq.

STAGE-1 (1200-1400 EST)
SEA BREEZE CONVERGENCE STAGE

Initial Sea Breeze
Convergence Zone

LAND SEA

East

Figure 24 - The conceptual model for the Stage-1, or the sea breeze convergence stage, of the convective-environmental interaction over southern Florida (on the XZ-cross section shown by the AB line in Fig. 11) during synoptically undisturbed days. Main points shown in this figure include: (1) embedded deep cumulus convection within the sea breeze convergence zone, (2) a vertically stretched solenoidal circulation, (3) divergence and vorticity maxima coincide, and (4) the convective downdraft cooling effect is not yet significant.

50

Figure 25 - The Stage-1 horizontal divergence (10^{-4} s^{-1}, top) and vertical vorticity (10^{-4}, s^{-1}, bottom) at 9 m.

STAGE-2 (1400-1600 EST)

CONVECTIVE DOWNDRAFT COOLING STAGE
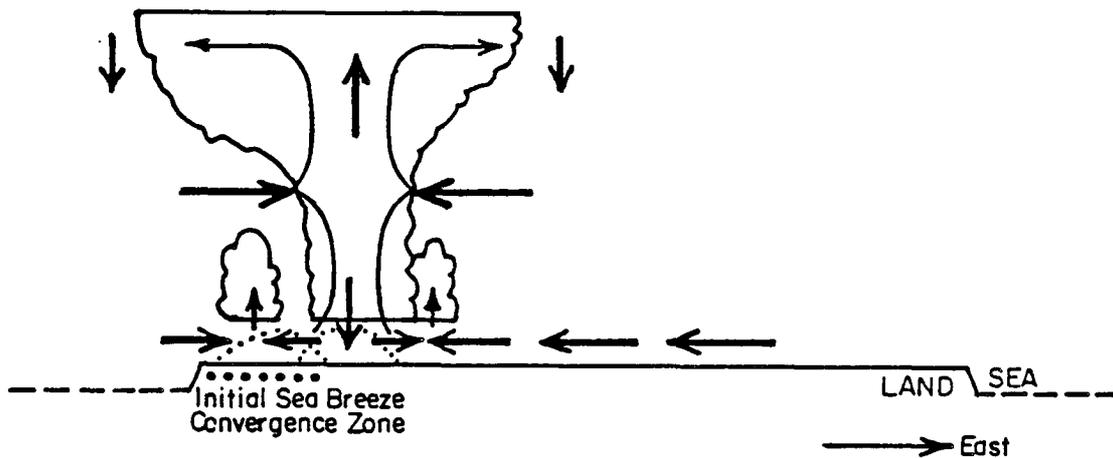
Figure 26 - Same as Fig. 24 but for the Stage-2, or the convective downdraft cooling stage. Main points shown in this figure include: (1) an upwind propagation, (2) midtropospheric convergence, (3) a "four-cell" vertical circulation pattern, (4) mesoscale upward and downward motions, and (5) a phase shift between divergence and vorticity maxima.
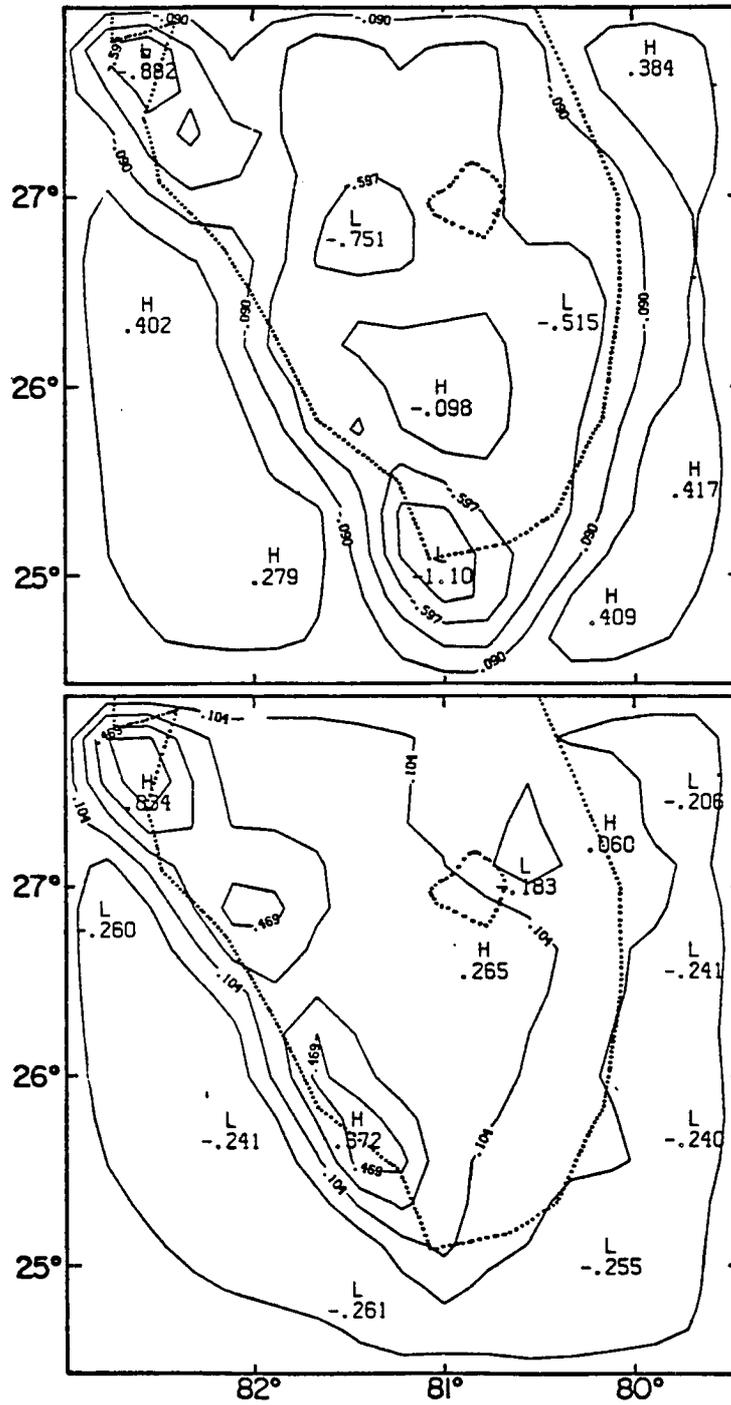
Figure 27 - Same as Fig. 25 but for the Stage-2.

STAGE-3 (1600-1800 EST)
DECAYING STAGE

Figure 28 - Same as Fig. 24 but for the Stage-3, or the decaying stage. Main points shown in this figure include: (1) mesoscale weaker upward and downward motions, (2) a decaying sea breeze, (3) lower-tropospheric drying, and (4) surface convergence farther away from deep convection.